



#### Available online at www.sciencedirect.com

## **ScienceDirect**

Comput. Methods Appl. Mech. Engrg. 313 (2017) 406-432

Computer methods in applied mechanics and engineering

www.elsevier.com/locate/cma

# An updated-Lagrangian damage mechanics formulation for modeling the creeping flow and fracture of ice sheets

Stephen Jiménez<sup>a</sup>, Ravindra Duddu<sup>a,\*</sup>, Jeremy Bassis<sup>b</sup>

<sup>a</sup> Department of Civil and Environmental Engineering, Vanderbilt University, Nashville, TN, United States <sup>b</sup> Department of Atmospheric, Oceanic, and Space Sciences, University of Michigan, Ann Arbor, MI, United States

Received 4 May 2016; received in revised form 6 September 2016; accepted 26 September 2016 Available online 5 October 2016

#### Highlights

- The updated-Lagrangian damage mechanics formulation is appropriate for ice sheet fracture simulation over long time scales.
- The nonlinear Stokes flow model is consistent with the Maxwell viscoelastic model over short time scales of crevasse propagation.
- The mixed P3–P1 and P2–P1 finite elements are both stable and predict the same crevasse growth rates.
- Explicit-integral and implicit-gradient nonlocal damage approaches are equivalent and alleviate mesh sensitivity.
- The damage control strategy using the discontinuous function  $\psi(D)$  is a viable alternative to the element removal procedure.

#### Abstract

An updated-Lagrangian formulation is developed to model the incompressible Stokes (creeping) flow and fracture of ice sheets using both explicit-integral and implicit-gradient nonlocal damage approaches. The governing equations of incompressible nonlinearly viscous Stokes flow assuming the plane strain approximation are discretized using high-order mixed finite elements over the current reference domain. The discretized nonlinear system is solved using a Picard iteration scheme, and a mesh update method is employed to obtain the updated reference domain at every time step. Fracture (crevasse) initiation and propagation is modeled using a scalar (isotropic) damage variable, and damage control or element removal strategies are implemented to avoid numerical accuracy and convergence issues arising from fully damaged finite elements near the crevasse tip. The formulation is implemented in the open-source finite element software FEniCS, and the relevant numerical algorithms are detailed. Numerical verification and benchmark studies based on manufactured nonlinear Stokes solutions and constant velocity and gravity-driven creep flow experiments are conducted to establish the viability of the formulation. We demonstrate that crevasse propagation rates obtained from nonlinear Stokes and Maxwell viscoelastic models are in good agreement over short time scales (days), so it is reasonable to neglect the elastic effects and employ the Stokes model to simulate iceberg calving. Furthermore, we demonstrate that over long time scales (months) the updated-Lagrangian Stokes formulation is more physically accurate than the total Lagrangian Maxwell viscoelastic formulation because the former accounts for the domain geometry changes. To conclude, the merit of the

E-mail address: ravindra.duddu@vanderbilt.edu (R. Duddu).

<sup>\*</sup> Corresponding author.

proposed formulation is two-fold: first, it is computationally more efficient than the Maxwell viscoelastic model; and second, it accounts for finite strain creep deformations accruing over long time scales. © 2016 Elsevier B.V. All rights reserved.

Keywords: Stokes flow; Ice mechanics; Nonlocal damage; Galerkin mixed finite element; Creep fracture; Viscoelasticity

#### 1. Introduction

Fracture initiation and propagation affect the stability of ice sheets by accelerating their flow, promoting iceberg calving, and triggering catastrophic collapse of glaciers and ice shelves [1,2]. Modeling and simulation of creep fracture (damage) mechanisms and its relation to the flow behavior (rheology) of ice sheets/shelves can be useful in providing reliable estimates for mass loss from ice sheets, a key component of sea level. Current numerical ice sheet/shelf models used to study their stability employ empirical calving laws and do not account for the physics of fracture, severely limiting their predictive capability and reliability. The purpose and scope of this paper is to present an updated-Lagrangian damage mechanics formulation to enable physically accurate modeling of fracture evolution in glaciers and land ice sheets that are slowly but continuously deforming under the force of gravity. In the proposed formulation, we employ high-order mixed finite element discretizations for the solution of nonlinear incompressible Stokes flow equations and nonlocal damage approaches that ensure stability and mesh-insensitivity of numerical simulations.

Over the long time scales of glacier and ice sheet evolution (decades to centuries or longer) it is well established that the rheology of ice is well represented by a non-Newtonian shear thinning (nonlinearly viscous) fluid, using the power law creep equation known as the Glen's law [3-6] in glaciology. By incorporating this viscous rheology, several studies have established that the three-dimensional (3D) nonlinear incompressible Stokes equations (hereafter referred to as the Stokes equations for brevity) provide the most accurate description of momentum balance for modeling the flow of glaciers, compared to other approaches (see [7,8] for more references and verification studies). The advantage of using the Stokes equations is that we can accurately model glacier flow by accounting for the topography (or geometry) and complex basal boundary conditions at the ice-bedrock interface [9]. Moreover, recent advances in higher-order finite element discretization and scalable solvers for the solution of Stokes equations [10,11] enable us to utilize the coverage and spatial resolution of ice sheet geometry data available from high-resolution satellite imagery and simulate the dynamics of large glaciers or even the entire Antarctic land ice sheet. However, to use the Stokes formulation to predict glacier and ice sheet evolution we need to account for iceberg calving, and this requires that we also simulate the damage induced crevasse formation and propagation, occurring on much shorter time scales (days to months). Furthermore, due to the vast separation of time scales associated with flow and fracture processes, the time between fracture inception and iceberg calving events associated with complete failure can exceed decades and sometimes centuries. This is particularly challenging because it requires us to couple the solid mechanics of creep fracture with the fluid mechanics of viscous flow in a consistent yet computationally feasible manner. To address this, we propose a new updated-Lagrangian formulation that can consistently describe short and long time scale behavior.

To account for the physical mechanisms of creep fracture behind crevasse propagation and iceberg calving, researchers have often relied upon theoretical models based on linear elastic fracture mechanics (LEFM) (see e.g., [12–15]) or Nye-zero stress models (see e.g., [16–18]). These models (viz., LEFM and Nye-zero stress) assume that ice behaves like a brittle elastic solid and represent fractures as sharp interfaces initiating and propagating from preexisting defects (either starter cracks or notches); however, this is inconsistent with the creeping flow and fracture behavior of ice evident from laboratory experiments, field investigations, and satellite observations. As an alternative to the LEFM approach, Pralong et al. [19] have proposed a Eulerian damage mechanics approach based on nonlinear Stokes flow and continuum creep damage mechanics. While this approach describes the physics of flow (deformation) and fracture of ice bodies, it suffers from numerical accuracy issues of pathological mesh dependence and directional mesh bias associated with local damage models and artificial dissipation of damage associated with advection in a Eulerian description. To overcome such numerical issues, Duddu et al., [20–23] modeled ice as a Maxwell-type viscoelastic solid (see the online supplementary material Section 1) in conjunction with a continuum damage mechanics approach using a Lagrangian finite element method. The Maxwell viscoelastic model is well calibrated and validated against laboratory experiments on polycrystalline ice in [20], and the nonlocal integral damage approach within a total

Lagrangian formulation is shown to alleviate mesh sensitivity issues in [21]; however, this pure displacement (one-field) formulation could suffer from numerical instabilities (e.g., oscillations in stress/pressure fields) when describing large incompressible viscous deformation combined with small elastic deformation. This issue may be resolved by introducing stabilization in the form of "hourglass" control and reduced integration techniques (see, e.g., [24,25]) or by using the B-type projection technique (see, e.g., [26]). Instead, we pursue a velocity–pressure (two-field) formulation, assuming Stokes flow, in conjunction with nonlocal damage mechanics for simulating creep fracture of ice within a mixed Galerkin finite element framework.

It is well known that using equal-order interpolation of velocity and pressure fields in the mixed Galerkin finite element formulation of incompressible Stokes, Navier–Stokes, and Darcy flow problems is not stable and causes numerical "checkerboard" instability in the pressure field (see e.g., [27–30]). This numerical instability occurs because same-order interpolations for unknown variables do not satisfy the inf–sup condition, most popularly known as the Ladyzhenskaya–Babuška–Brezzi (LBB) stability condition [31–33]. To ensure numerical stability and optimal convergence, several methodologies have been proposed in the literature for enabling stable equal-order interpolation of velocity and pressure fields. An in-depth review of the various stabilized or enriched finite element methods can be found in [26,29]; herein, we wish to acknowledge a few important articles related to these methods: Streamline Upwind Petrov–Galerkin (SUPG, see, e.g., [34,35]), Galerkin Least Squares (GLS, see e.g., [36]), variational multiscale method (VMS, see e.g., [29,37–40]), bubble enriched finite element methods (see, e.g., [41,42]). An alternative, more straightforward strategy is to use different order interpolation for velocity and pressure variables, which is pursued in this paper in conjunction with triangular elements by using cubic and linear polynomials for interpolating velocity and pressure fields, respectively. Recently, we also employed different order interpolation for velocity and Jacobian determinant variables in conjunction with quadrilateral elements [43,44] to simulate large deformations in hyperelastic solids within a Eulerian framework.

An important aspect in ice sheet modeling is that we need to track the changes in the physical geometry (i.e., shape and the size) of the ice sheet domain due to large deformations accruing over decadal time scales. Typically, over such long times scales a Eulerian framework (see e.g., [19,45,46]) is employed, wherein domain boundaries are typically fixed and the material is advected out. While the advantage of the Eulerian formulation over the Lagrangian formulation is that it enables the efficient simulation of ice sheet flow without requiring remeshing, it cannot track changes in geometry of the domain and material discontinuities such as fracture and damage zones; therefore, it is not ideal for simulating the fracture of ice sheets. In this context, the primary goal of this work is three-fold: first, to present a novel mixed finite element implementation of the updated-Lagrangian formulation of the incompressible Stokes flow [47] in conjunction with a mesh-update procedure, which can be ideal for modeling flow and fracture in ice sheets on long times scales; second, to demonstrate that the nonlinearly viscous Stokes flow constitutive model reproduces the results of the previously established Maxwell-viscoelastic constitutive model with to respect crevasse depths and glacial displacement over short time scales (days to months); and third, to conduct numerical verification and mesh convergence studies along with a comparison of gradient and integral nonlocal models for time dependent creep damage. The secondary goal of this work is to present computational algorithms and strategies for simulating crevasse propagation. To the best of our knowledge, there exist no other formulations in the literature that incorporate nonlocal creep damage into nonlinear Stokes rheology to simulate fracture initiation and propagation. The rest of this paper is organized as follows: in Section 2 we present the governing equations of the Stokes flow rheological model for damaged ice; in Section 3 we discuss the solution strategy and finite element implementation of the new formulation in the open-source software FEniCS along with detailed algorithms; in Section 4 we provide numerical examples to verify and compare the new formulation with a manufactured Stokes solution and the previously established Maxwell viscoelastic model (see the online supplementary material Section 1), including constant velocity and gravity-driven creep flow tests; and finally, in Section 5 we offer some concluding remarks.

#### 2. Model formulation

In this section, we present the details of the rheological model for damaged ice used to describe the deformation flow and creep fracture of ice-sheets and ice-shelves. We first explain our notation for variables, the domain configurations and kinematics of the continuum. We next review the key concepts of the nonlocal continuum damage model for temperature-dependent creep fracture previously presented in [20,21] and propose a modification to consider isotropic damage evolution only under a tensile state of stress. Finally, we present the strong and weak forms

of the governing equations of the Stokes flow model, assuming that ice behaves as a non-Newtonian (or nonlinearly viscous) fluid, including the effects of creep damage on its viscosity.

#### 2.1. Notation

All model equations are presented in indicial notation; for example, vectors are denoted as  $\mathbf{a} = a_i \hat{\mathbf{e}}_i$  with components  $a_i$  and orthogonal basis vectors  $\hat{\mathbf{e}}_i$  of the Cartesian coordinate system. Similarly, second-order tensors are denoted by the dyadic notation as  $\mathbf{A} = A_{ij}\hat{\mathbf{e}}_i \otimes \hat{\mathbf{e}}_j$  with components  $A_{ij}$ . The equations are presented in three-dimensional space with the spatial indices  $i, j \in \{1, 2, 3\}$ , although the simulations are conducted assuming two-dimensional plane strain approximation. We adopt Einstein's convention where repeated spatial indices imply summation. To denote the value of a vector or tensor at time step n we use the left superscript; for iterative procedures we use m as the counter and set it as a left subscript surrounded by parentheses; and we reserve the right superscript for exponents (italicized) or descriptors (unitalicized). For example,  $\binom{n}{(m)} \varepsilon_{ij}^e$  denotes the elastic (e) component of the second-order strain tensor  $\varepsilon_{ij}$  at time step n and iteration m. Any symbol written without the left superscript is assumed to be at time step n.

## 2.2. Domain description

We employ the updated-Lagrangian description, rather than a total Lagrangian or Eulerian description, to efficiently simulate the viscous flow and fracture of ice. In the updated-Lagrangian description, the positions of the material points in the continuum and their motion are described using a reference configuration that dynamically evolves as the domain deforms. For this reason, we will distinguish the *initial* reference configuration from *current* and *updated* reference configurations, as illustrated in Fig. 1. The *initial* reference configuration is denoted by  ${}^{0}\Omega$  and contains all the material points with initial spatial coordinates  ${}^{0}x$ . The current spatial coordinates of the material points in the domain  ${}^{n}\Omega$  are denoted by  ${}^{n}x = {}^{n}x_{i}\hat{e}_{i}$ . At any given time step n, the *current* reference domain  ${}^{n}\Omega$  is bounded by the union of the Dirichlet and Neumann boundaries  ${}^{n}\Gamma^{D}$  and  ${}^{n}\Gamma^{N}$ , respectively. The *updated* reference configuration is defined by the domain  ${}^{n+1}\Omega$  after the material points are translated using a displacement increment  ${}^{n}\Delta u$  between time steps n and n+1. The kinematics of the moving continuum and the procedure for calculating  $\Delta u$  are described in the following section.

#### 2.3. Kinematics

The current velocity of material particles in the domain  ${}^{n}\Omega$  is denoted by  $v(x,t) = v_{i}\hat{e}_{i}$  and the corresponding strain-rate is defined as

$$\dot{\epsilon}_{ij} = \frac{1}{2} \left( \frac{\partial v_i}{\partial x_j} + \frac{\partial v_j}{\partial x_i} \right). \tag{1}$$

In the literature, the above quantity is commonly referred to as the *rate of deformation* tensor. Generally, in the total Lagrangian description the displacement u of each material point in the current configuration  ${}^{n}\Omega$  is defined by the difference between its current and initial spatial coordinates

$$u_i = x_i - {}^0x_i. (2)$$

In the updated-Lagrangian framework, the displacement of material particles between  ${}^n\Omega$  to  ${}^{n+1}\Omega$  is defined using the displacement increment as

$$\Delta u_i = {}^{n+1}u_i - u_i = {}^{n+1}x_i - x_i. \tag{3}$$

The displacement increment  ${}^{n}\Delta u$  can be obtained by integrating the flow velocity over time [47]

$$\Delta u_i = \int_{n_t}^{n+1} v_i(\mathbf{x}, \tau) d\tau. \tag{4}$$

Note that between the times  ${}^nt$  and  ${}^{n+1}t$  the domain continuously moves with a variable velocity field  $v_i(x,\tau)$  from  ${}^n\Omega$  with known coordinates x to the updated configuration  ${}^{n+1}\Omega$  with unknown coordinates  ${}^{n+1}x$  [48]; therefore,

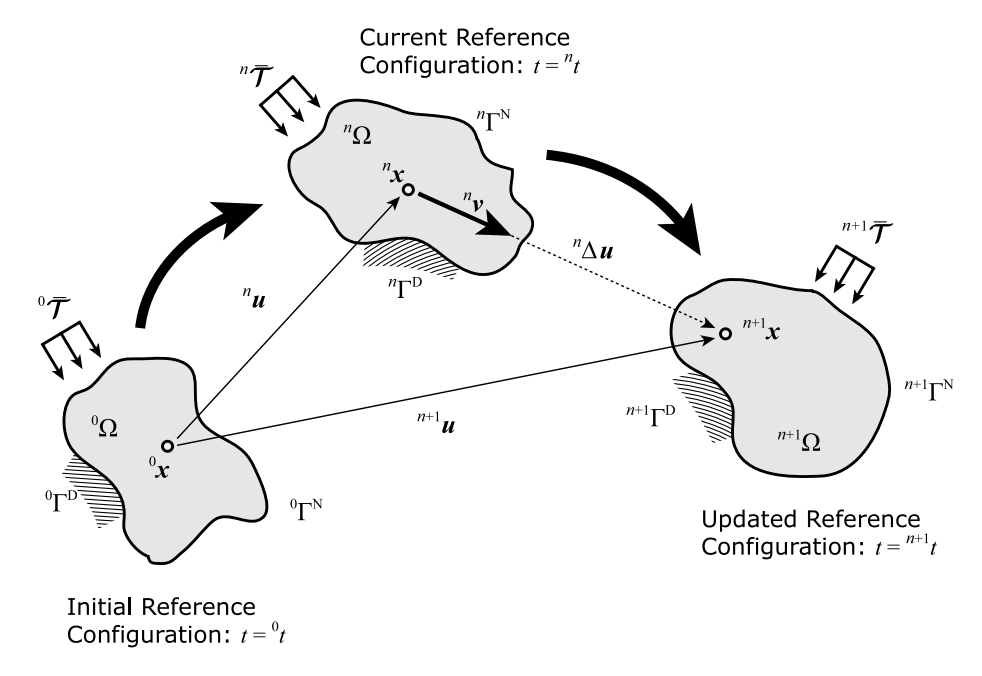


Fig. 1. Illustration of reference domain configurations in the updated-Lagrangian description (redrawn from [47]). The initial, current, and updated reference configurations are defined the by domains indicated by  ${}^0\Omega$ ,  ${}^n\Omega$ , and  ${}^{n+1}\Omega$ , respectively. The symbols  ${}^{\Gamma}$  and  ${}^{\Gamma}$  respectively denote the Dirichlet and Neumann boundaries, and  $\tilde{\mathcal{T}}$  is a vector of applied tractions.

an iterative scheme is required to account for the change in reference configuration [47]. However, assuming small changes in particle velocities during the time increment  $\Delta t = {}^{n+1}t - {}^nt$ , we approximate the displacement increment and update the nodal coordinates as

$$\Delta u_i = {}^{n+1}v_i(\mathbf{x}, t) \ \Delta t, \tag{5}$$

$$^{n+1}x_i = {}^nx_i + \Delta u_i. \tag{6}$$

The procedure for computing velocity  $^{n+1}v_i(x, t)$  is detailed in Section 2.6.

#### 2.4. Nonlocal creep continuum damage model

The continuum damage model for creep fracture is built on the principle of effective stress [49,50] and the hypothesis of strain equivalence [51], which states that "the strain associated with a damaged state under the applied stress is equivalent to the strain associated with its undamaged state under the effective stress". Here, we assume damage evolves isotropically under tension, so it is represented by a scalar variable  $D \in [0, 1]$ , where D = 0 and D = 1 represent an undamaged (virgin) and a fully damaged state, respectively, at a material point in the continuum. The effective Cauchy stress tensor  $\tilde{\sigma}_{ij}$  can be defined in terms of the actual Cauchy stress tensor  $\sigma_{ij}$  as

$$\widetilde{\sigma}_{ij} = \frac{\sigma_{ij}}{(1-D)}. (7)$$

The process of creep damage is generally associated with progressive degradation due to the growth of microcracks and microvoids [52,53]. To account for the time-dependent degradation mechanisms, the local rate of evolution of damage  $\dot{D}^{\rm loc}$  at a material point is phenomenologically defined by a dynamic damage evolution function f as

$$\dot{D}^{\text{loc}} = \frac{\partial D^{\text{loc}}}{\partial t} = \begin{cases} f(\sigma_{ij}, D), & \text{if } \sigma_{kk} \ge 0, \\ 0, & \text{if } \sigma_{kk} < 0. \end{cases}$$
 (8)

**Remark 1.** Laboratory experimental studies indicate that ice exhibits tension–compression asymmetry in its mechanical response to loading. While damage evolution in ice under tension is clearly observed to be due to the growth and

coalescence of microcracks and microvoids, damage evolution under compression is also complicated by recrystal-lization process, as noted in [54]. Because ice is much stronger in compression than in tension, crevasses (fractures) are always observed in regions under tensile stress states; so, we only consider damage evolution under tension.

**Remark 2.** The isotropic damage variable D can be physically interpreted as the ratio of the area of spherical microvoids to the total area along a cross-sectional cut of a representative volume element at a material point [55]; therefore, in Eq. (8), damage growth due to nucleation and growth of spherical micro-voids is permitted only when the stress state at a material point is predominantly tensile, that is, when the hydrostatic stress  $\sigma_{kk} > 0$ .

We next define the damage evolution function f for the generalized multi-axial stress state as [56]

$$f = \hat{B} \frac{\langle \chi \rangle^r}{(1 - D)^{k_\sigma}},\tag{9}$$

where  $\hat{B}$  and r are material parameters controlling the damage growth rate;  $k_{\sigma}$  is a stress-dependent term;  $\langle \cdot \rangle$  represents the Macaulay brackets, such that  $\langle \chi \rangle = \max\{\chi, 0\}$ ; and the effective Hayhurst stress  $\chi$  is defined as [57]

$$\chi = \alpha \widetilde{\sigma}^{(1)} + \beta \widetilde{\sigma}^{V} + (1 - \alpha - \beta) \widetilde{\sigma}_{kk}. \tag{10}$$

In the above equation,  $\alpha$  and  $\beta$  are material parameters corresponding to brittle and ductile crack growth mechanisms, respectively;  $\widetilde{\sigma}^{(I)}$  is the maximum principal stress in the effective space;  $\widetilde{\sigma}^{v}$  is the effective von Mises stress; and  $\widetilde{\sigma}_{kk}$  is the trace of the effective Cauchy stress tensor (i.e., the first invariant of the effective stress). Because  $\chi$  is a weighted average of stress invariants, it is invariant with coordinate transformation. The stress-dependent parameter  $k_{\sigma}$  is an experimentally calibrated parameter defined as

$$k_{\sigma} = k_1 + k_2 \sigma_{kk}$$
, if  $\sigma_{kk} \ge 0$ . (11)

The parameter  $k_{\sigma}$  accounts for the tertiary creep behavior, wherein the presence of pre-existing damage in polycrystalline ice accelerates crack growth rate under tension leading up to rupture.

## 2.4.1. Nonlocal integral damage

To ensure thermodynamic consistency and to alleviate mesh dependence issues with the numerical implementation of local damage models [58–62], we define a nonlocal damage rate  $\dot{D}$  at a specific material point at spatial location x in the reference configuration  $\Omega$  as

$$\dot{D}(\mathbf{x}) = \frac{\int_{\Omega} \Phi\left(\mathbf{x} - \hat{\mathbf{x}}\right) \dot{D}^{\text{loc}}\left(\hat{\mathbf{x}}\right) d\hat{\mathbf{x}}}{\int_{\Omega} \Phi\left(\mathbf{x} - \hat{\mathbf{x}}\right) d\hat{\mathbf{x}}},\tag{12}$$

where  $\hat{x} = \hat{x}_i \hat{e}_i$  denotes the spatial coordinates of any material point in  $\Omega$ , and  $\Phi$  can be selected as either Gaussian or Green's weighting function defined by

$$\Phi\left(\mathbf{x} - \hat{\mathbf{x}}\right) = \begin{cases}
\exp\left(-\kappa \frac{\|\mathbf{x} - \hat{\mathbf{x}}\|^2}{l_c^2}\right) & \text{(Gaussian),} \\
\exp\left(-2\sqrt{\kappa} \frac{\|\mathbf{x} - \hat{\mathbf{x}}\|}{l_c}\right) & \text{(Green's).}
\end{cases}$$
(13)

In the above equation, the shape parameter  $\kappa$  is a positive constant and  $l_c$  is a chosen nonlocal length scale for purely numerical reasons. In our simulation studies, we take  $l_c=10$  m and  $\kappa=2$ , and all other damage model parameters and their values are listed in Table 1. The numerical implementation of the nonlocal integral is detailed in Section 3.2.

#### 2.4.2. Implicit gradient damage

We next present an implicit gradient formulation for computing the nonlocal damage rate [63,64]. The implicit gradient can be simply derived by expanding the local damage rate  $\dot{D}^{loc}$  as a Taylor series about  $\hat{x}$  as

$$\dot{D}^{\text{loc}}(\hat{\mathbf{x}}) = \dot{D}^{\text{loc}}(\mathbf{x}) + \frac{\partial \dot{D}^{\text{loc}}}{\partial x_i} \left( \hat{x}_i - x_i \right) + \frac{1}{2!} \frac{\partial \dot{D}^{\text{loc}}}{\partial x_i \partial x_j} \left( \hat{x}_i - x_i \right) \left( \hat{x}_j - x_j \right) + \cdots$$
(14)

F 5					
Parameter	Value	Units			
$\hat{B}$	$5.23 \times 10^{-7}$	$MPa^{-r} s^{-1}$			
r	0.43	_			
$k_1$	-2.63	_			
$k_2$	7.24	$MPa^{-1}$			
α	0.21	_			
β	0.63	_			
$l_c$	10	m			
κ	2	-			

Table 1
Damage law parameters obtained from [21].

By substituting the above expression and the kernel function (Eq. (13)) into Eq. (12), the nonlocal damage rate can be defined as

$$\dot{D}(\mathbf{x}) = \dot{D}^{\text{loc}}(\mathbf{x}) + \frac{l_c^2}{4\kappa} \frac{\partial^2}{\partial x_i^2} \dot{D}^{\text{loc}}(\mathbf{x}) + \frac{l_c^4}{32\kappa^2} \frac{\partial^4}{\partial x_i^2 \partial x_j^2} \dot{D}^{\text{loc}}(\mathbf{x}) + \cdots$$
(15)

The partial differential equation corresponding to the implicit gradient formulation can be obtained by taking the Laplacian of Eq. (15), multiplying by  $\frac{l_c^2}{c}$ , subtracting that expression from Eq. (15) and then neglecting higher-order gradient terms to yield a simple form as follows:

$$\dot{D} - \frac{l_c^2}{4\kappa} \frac{\partial^2}{\partial x_i^2} \dot{D} = \dot{D}^{\text{loc}}.$$
 (16)

The numerical implementation of the implicit gradient formulation is provided in Section 3.2.

## 2.5. Rheology of damaged ice

The rheological model describes the nonlinear viscous flow behavior of damaged ice based on Glen's flow law [3,65]. Assuming polycrystalline ice to be isotropic and incompressible, the viscous strain rate of damaged ice is given by

$$\dot{\epsilon}_{ij} = A(\widetilde{\tau}^{\text{eq}})^{N-1} \widetilde{\tau}_{ij} \tag{17}$$

where  $\tilde{\tau}_{ij}$  is the effective deviatoric stress, coefficient A and exponent N are viscous flow parameters, and the effective equivalent deviatoric stress  $\tilde{\tau}^{eq}$  is defined in terms of the second invariant as

$$\widetilde{\tau}^{\text{eq}} = \sqrt{\frac{1}{2}\widetilde{\tau}_{ij}\widetilde{\tau}_{ij}}.$$
(18)

Note that the viscous flow of ice is faster at higher temperatures, and this is accounted for by defining an Arrheniustype relation for the temperature dependence of the viscous flow coefficient A [6]. In this study, however, we conduct all the simulations using the material properties of ice at a constant temperature T = -10 °C, as given in Table 2.

The constitutive law in Eq. (17) can be inverted and rewritten as

$$\widetilde{\tau}_{ij} = B \left( \dot{\epsilon}^{\text{eq}} \right)^{\frac{1}{N} - 1} \dot{\epsilon}_{ij},\tag{19}$$

where  $B = A^{-1/N}$  and the equivalent strain rate is

$$\dot{\epsilon}^{\text{eq}} = \sqrt{\frac{1}{2}\dot{\epsilon}_{ij}\dot{\epsilon}_{ij}}.$$

Table 2 Material properties of ice at -10 °C obtained from [6,21].

Property	Value	Units	
В	111.8	MPa s <sup>1/3</sup>	
N	3	-	
$ ho_{ m ice}$	917	$kg/m^3$	

Eq. (19) represents a generalized constitutive flow law for a damaged non-Newtonian fluid-like material as given by

$$\tau_{ij} = 2(1-D)\eta\dot{\epsilon}_{ij},\tag{21}$$

where the nonlinear viscosity  $\eta = \frac{1}{2}B\left([\dot{\epsilon}^{\rm eq}]^2 + \gamma\right)^{\frac{1-N}{2N}}$  and  $\gamma = 10^{-14}~{\rm s}^{-2}$  is a small regularization parameter introduced to avoid problems with the nonlinear solver when using a zero or constant velocity initial guess (i.e., when  $\dot{\epsilon}^{\rm eq} = 0$ ) [66]. The Cauchy stress tensor  $\sigma_{ij}$  can then be obtained as

$$\sigma_{ij} = \tau_{ij} - p\delta_{ij}. \tag{22}$$

In the above equation,  $p = -\frac{1}{3}\sigma_{kk}$  is the pressure and  $\delta_{ij}$  represents the Kronecker's delta where  $\delta_{ij} = 1$  if i = j, and  $\delta_{ij} = 0$  otherwise.

#### 2.6. Strong form

The strong form of the governing equations is specified by the incompressible Stokes equations describing the creeping flow of the continuum based on momentum balance. In this two-field formulation, the unknown fields are the vector velocity field  $^{n+1}v = v \binom{n+1}{x}, ^{n+1}t$  and the scalar pressure field  $^{n+1}p = p \binom{n+1}{x}, ^{n+1}t$  which are defined as functions of the updated reference coordinates  $^{n+1}x$  over the updated configuration  $^{n+1}\Omega$ . For incompressible, isotropic fluids, the strong form of the Stokes flow equations is written as

$$\frac{\partial^{n+1}\tau_{ij}}{\partial^{n+1}x_{j}} - \frac{\partial^{n+1}p}{\partial^{n+1}x_{i}} + \psi(^{n}D)^{n+1}b_{i} = 0$$

$$\psi(^{n}D)\frac{\partial^{n+1}v_{i}}{\partial^{n+1}x_{i}} = 0$$
on  $^{n+1}\Omega$ ,
$$(23)$$

where  $\tau_{ij}$  is the deviatoric stress tensor, and  $b_i$  is the external force vector. The function  $\psi(^nD)$  is incorporated to relax the incompressibility constraint and disregard the density of fully damaged material points, and is taken as

$$\psi(^{n}D) = \begin{cases} 1, & \text{if} \quad ^{n}D < D^{\max}, \\ \xi, & \text{if} \quad ^{n}D = D^{\max}, \end{cases}$$

$$(24)$$

where  $D^{\max} \approx 1$  is the prescribed maximum value for damage and  $\xi = 10^{-16} \approx 0$  is chosen as a very small number to avoid rank deficiency of the tangent matrix. We assume  $\psi(D)$  as a discontinuous (step) function, as opposed to a continuous function, because we wish to relax incompressibility and disregard density only after the macro-crack appears (i.e.,  $^nD = D^{\max}$ ) and not during micro-crack nucleation and growth; however, the mechanics of damaged (viscous) ice is a complicated issue, so the discontinuous form in Eq. (24) is considered for purely numerical reasons in this study.

**Remark 3.** While it may be physically consistent to assume that fully damaged ice no longer behaves like an incompressible medium, disregarding the density of damaged ice may not be physically consistent because it can remain in the crevasse as rubble or ice mélange [67] and exert cryostatic stress due to self-weight. Furthermore, meltwater can now percolate into the fully damaged zone and exert hydrostatic pressure along the edges of the crack (or crevasse) [23].

Remark 4. From a computational standpoint, applying the body force due to gravity while the viscosity of damaged ice tends to zero is problematic because it leads to excessive displacements and distortions in damaged regions of the finite element mesh; therefore, we introduce  $\psi(D)$  into the body force term in Eq. (24) to disregard body force at fully damaged material points. Modeling fully damaged ice either as an anisotropic material with tension–compression asymmetry [20] or as a granular material using the Mohr–Coulomb failure theory [68] could overcome this problem; however, the numerical implementation would become very cumbersome as we need to switch between rheological models based on the damaged state.

Upon substituting the kinematic equation (Eq. (1)) and constitutive relation (Eq. (21)), the strong form can be rewritten in terms of velocity, effective pressure, and prior damage in the updated configuration as

$$\frac{\partial}{\partial^{n+1}x_{j}} \left\{ \left[ 1 - {}^{n}D \right] \eta \left( {}^{n+1}v \right) \left[ \frac{\partial^{n+1}v_{i}}{\partial^{n+1}x_{j}} + \frac{\partial^{n+1}v_{j}}{\partial^{n+1}x_{i}} \right] \right\} - \left[ 1 - {}^{n}D \right] \frac{\partial^{n+1}\widetilde{p}}{\partial^{n+1}x_{i}} + \psi \left( {}^{n}D \right)^{n+1}b_{i} = 0$$

$$\psi \left( {}^{n}D \right) \frac{\partial^{n+1}v_{i}}{\partial^{n+1}x_{i}} = 0$$
on  $^{n+1}\Omega$ , (25)

together with the Dirichlet and Neumann boundary conditions

$${}^{n+1}v_i = {}^{n+1}\bar{v}_i \text{ on } {}^{n+1}\Gamma^{D},$$

$${}^{n+1}\sigma_{ij} {}^{n+1}\hat{n}_j = {}^{n+1}\bar{\mathcal{T}}_i \text{ on } {}^{n+1}\Gamma^{N},$$
(26)

where  ${}^{n+1}\bar{\nu}_i$  are applied velocities,  ${}^{n+1}\bar{\mathcal{T}}_i$  are applied tractions, and  ${}^{n+1}\hat{n}_j$  is an outward unit normal vector to the surface of the boundary. In Eq. (25), the viscosity  $\eta$  is a nonlinear function of the velocity defined as,  $\eta$  ( ${}^{n+1}\nu$ ) =  $\frac{1}{2}B\left([{}^{n+1}\dot{\epsilon}^{\rm eq}]^2+\gamma\right)^{\frac{1-N}{2N}}$ , where  ${}^{n+1}\dot{\epsilon}^{\rm eq}$  is defined in Eq. (20); and the effective pressure  $\widetilde{p}=(1-D)^{-1}p$ .

## 2.7. Weak form

The weak form of Eq. (25) is obtained by incorporating test functions w and q, integrating by parts, and then applying Gauss's theorem. The weak or variational form can be stated as follows:

Find  $^{n+1}v \in \mathcal{V}$  and  $^{n+1}\widetilde{p} \in \mathcal{S}$  such that  $\forall w \in \mathcal{V}$  and  $q \in \mathcal{S}$ :

$$\int_{n+1}^{\infty} \frac{\partial w_{i}}{\partial n+1} \left\{ \left[ 1 - {}^{n}D \right] \eta \left( {}^{n+1}v \right) \left[ \frac{\partial n+1}{\partial n+1} v_{i} + \frac{\partial n+1}{\partial n+1} v_{i} \right] \right\} d\Omega 
- \int_{n+1}^{\infty} \left[ 1 - {}^{n}D \right] \frac{\partial w_{i}}{\partial n+1} {}^{n+1} \widetilde{p} d\Omega - \int_{n+1}^{\infty} \psi \left( {}^{n}D \right) w_{i} {}^{n+1}b_{i} d\Omega 
- \int_{n+1}^{\infty} w_{i} {}^{n+1} \overline{T}_{i} d\Gamma = 0$$

$$\int_{n+1}^{\infty} \psi \left( {}^{n}D \right) q \frac{\partial n+1}{\partial n+1} v_{i} d\Omega = 0$$
(27)

where V and S are vector and scalar function spaces, respectively. Because the updated coordinates  $^{n+1}x$  are unknown at time step n, solving the above weak formulation will require an implicit scheme, which can be cumbersome.

**Remark 5.** An alternative weak form can be stated in the current reference configuration  ${}^{n}\Omega$  in terms of the Green–Lagrange strain-rate tensor  $\dot{E}_{ij}$  and the second Piola–Kirchhoff stress tensor  $S_{ij}$ . In this alternative form, all the gradient quantities are written in terms of the (known) current reference coordinates  ${}^{n}x$ ; however, the computation of the unknown displacement increment  ${}^{n}\Delta u = {}^{n+1}x - {}^{n}x$  between configurations  ${}^{n+1}\Omega$  and  ${}^{n}\Omega$  necessitates an iterative procedure, which can be cumbersome. Furthermore, the consistent tangent corresponding to this alternative weak form is much more complicated, as described in [47].

To simplify the numerical implementation, we express the above weak form over the current reference configuration  ${}^n\Omega$  (see [47] for a detailed derivation) and assume that the displacement increment gradient  $\frac{\partial \Delta u_i}{\partial {}^n x_j} \ll 1$  and deformation gradient  $F_{ij} = \frac{\partial {}^{n+1} x_j}{\partial {}^n x_j} \approx 1$ . Consequently, for small time increments  $\Delta t$ , we can now state the approximate weak form over the current reference configuration  ${}^n\Omega$  as follows:

Find  $^{n+1}v \in \mathcal{V}$  and  $^{n+1}\widetilde{p} \in \mathcal{S}$  such that  $\forall w \in \mathcal{V}$  and  $q \in \mathcal{S}$ :

$$\int_{n\Omega} \frac{\partial w_{i}}{\partial^{n} x_{j}} \left\{ \left[ 1 - {}^{n} D \right] \eta \left( {}^{n+1} v \right) \left[ \frac{\partial^{n+1} v_{i}}{\partial^{n} x_{j}} + \frac{\partial^{n+1} v_{j}}{\partial^{n} x_{i}} \right] \right\} d\Omega 
- \int_{n\Omega} \left[ 1 - {}^{n} D \right] \frac{\partial w_{i}}{\partial^{n} x_{i}}^{n+1} \widetilde{p} d\Omega - \int_{n\Omega} \psi \left( {}^{n} D \right) w_{i}^{n} b_{i} d\Omega - \int_{n\Gamma^{N}} w_{i}^{n} \overline{\mathcal{T}}_{i} d\Gamma = 0 
\int_{n\Omega} \psi \left( {}^{n} D \right) q \frac{\partial^{n+1} v_{i}}{\partial^{n} x_{i}} d\Omega = 0$$
on  ${}^{n} \Omega$ . (28)

In essence, the above approximate weak form reads almost exactly like the one in Eq. (27), if we assume  $\frac{\partial^n \Delta u_k}{\partial^n x_i} \ll 1$ , so that

$$\frac{\partial}{\partial^{n+1}x_j} \approx \frac{\partial}{\partial^n x_j},\tag{29}$$

and the relevant strain rate tensor  $^{n+1}\dot{\epsilon}_{ij}$  can now be approximated as

$$^{n+1}\dot{\epsilon}_{ij} \approx \frac{1}{2} \left[ \frac{\partial^{n+1}v_i}{\partial^n x_j} + \frac{\partial^{n+1}v_j}{\partial^n x_i} \right]. \tag{30}$$

The advantage in using the approximate weak form in Eq. (28) is that it can be directly solved over the current reference configuration to obtain velocity and pressure fields, and then the mesh update procedure can be implemented separately in a de-coupled manner by choosing an appropriate time step  $\Delta t$ , which leads to a computationally accurate yet tractable strategy.

**Remark 6.** The tensile strain rate corresponding to an expanding glacier is extremely small, typically, on the order of  $10^{-8}$  per second; this typically amounts to a flow velocity of a few meters per day for a typical glacier that spans tens to hundreds of kilometers in length and a few hundred meters or more in depth. Consequently, the longitudinal and transverse gradients in the displacement increment are small (given the large size scales of glaciers), so using the approximation in Eq. (29) is reasonable for creeping flow of glaciers.

## 3. Solution strategy

We now present the numerical strategy that combines the updated-Lagrangian description for simulating the viscous (Stokes) flow and the nonlocal integral approach for simulating creep fracture (damage) evolution. We employ a decoupled solution procedure that is explicit in time and consists of two sequential steps: (1) solve the variational form of the Stokes flow equations using a mixed finite element discretization, in conjunction with Picard iteration and mesh update schemes; (2) compute the damage increment using a nonlocal integral or gradient approach to establish the damage rate. During the Picard iteration scheme the flow velocity  $^{n+1}v_i$  and effective pressure  $^{n+1}\widetilde{p}$  fields are computed over the current reference configuration  $^n\Omega$ , while holding damage constant  $^nD$  at its previously computed value. Using the converged solutions for velocity and pressure, the Cauchy stress and the damage rate are subsequently computed to update damage. Thus, the damage update (step 2) is fully decoupled from the solution of Stokes flow problem (step 1). These two solution steps along with detailed algorithms are presented in the following sections.

**Remark 7.** Unlike the fully implicit damage models in the literature that are formulated for strain-dependent and rate- or time-independent damage functions (e.g., see [63]), creep damage in ice is a time-dependent process, and the damage rate is a highly nonlinear function of the full stress tensor [20]. Because the solution to the nonlinear Stokes equations is instantaneous (steady-state) and damage evolution is time-dependent and highly nonlinear, it is simpler

to use an explicit-time forward Euler scheme to update the damage separately; whereas, the implicit backward Euler scheme requiring a monolithic solve of the Stokes and damage evolution equations can become very cumbersome. For numerical accuracy and stability of the present scheme, we ensure that the damage increment is sufficiently small during each time step by choosing a suitable time increment according to Eq. (34).

#### 3.1. Solution of the variational form

We employ the finite element method to solve the variational form of the Stokes flow boundary value problem using FEniCS software. The advantage of FEniCS is that the Stokes flow problem can be directly specified in the variational form using the FEniCS Python application program interface (API). Based on the user-provided input, FEniCS interprets, assembles and solves the discretized linear system corresponding to the boundary value problem. The details of the full solution procedure are summarized in Algorithm 1. The procedure for setting up the problem in FEniCS<sup>1</sup> is detailed below:

- 1. The finite element mesh corresponding to the physical domain is provided as an XML file, which specifies triangular cells and the spacial locations of their vertices. The domain boundaries can then be defined by identifying the vertices belonging to the bottom, left, and right edges using the SubDomain class in FEniCS.
- 2. Next, the finite element function spaces corresponding to the pressure (scalar) and velocity (vector) variables are defined over the mesh using the FunctionSpace and VectorFunctionSpace Python objects, respectively. Because we adopt a standard Galerkin formulation, we use the function spaces belonging to the Lagrange element family.
- 3. Dirichlet boundary conditions on the velocity field are then defined using the DirichletBC Python object by providing the corresponding vector function space and the domain boundary.
- 4. Trial and test functions are introduced using the TrialFunction and TestFunction Python objects, respectively, for both scalar and vector function spaces. The weak form is simply provided by multiplying and adding the trial and test functions and their gradients to obtain the expression in Eq. (28); the gradient operator ∇ is provided by FEniCS as the built-in function nabla\_grad().
- 5. Due to the solution-dependent viscosity  $\eta$  ( $^{n+1}\nu$ ), Eq. (28) is highly nonlinear, and so we linearize the nonlinear system using a Picard iteration scheme, as detailed in Algorithm 2. The linearized system obtained at each Picard iteration is numerically solved using an iterative method by calling the solve() function, which takes the weak form and boundary conditions as input. An alternative to the Picard iteration scheme is the Newton's method [10], which can be implemented in FEniCS as detailed in the online supplementary material Section 3.

**Remark 8.** While the Newton's method has a faster rate of convergence than Picard iterations, we encountered convergence issues in FEniCS upon introduction of notches or damage zones into the nonlinear Stokes equations. We suspect that the automated assembly of the system Jacobian (tangent) matrix by FEniCS could be introducing interpolation errors that are affecting the overall convergence of the Newton's method; however, it could also be that the Newton's method is sensitive to the regularization parameter  $\gamma$  when the nonlinear Stokes equations are solved over non-convex domains. Perhaps implementing advanced algorithms with respect to the parameter  $\gamma$  could improve the convergence of the Newton's method, especially given the lack of a good initial guess [9].

Because FEniCS software currently only supports triangular finite elements, we select a computationally efficient and numerically (LBB) stable element for solving the incompressible Stokes equations, namely, the P3–P1 element, wherein the velocity  $^{n+1}v$  is resolved on a 10-noded triangle using third-order polynomial (cubic P3) interpolants and the effective pressure  $^{n+1}\tilde{p}$  is resolved on a 3-noded triangle using first-order polynomial (linear P1) interpolants. An illustration of the P3–P1 mixed element and the mesh configuration is given in Fig. 2. A stable alternative to the P3–P1 mixed element is the P2–P1 (Taylor–Hood) element, wherein the velocity is resolved using quadratic (P2) interpolation on a 6-noded triangle. Although the deviatoric stress can be calculated at the nodes of the P3 (or P2) element using the computed velocity field, we only calculate it at the nodes of the P1 element so that we can add it to the corresponding pressure to obtain the Cauchy stress. The damage variable is also interpolated using the P1

<sup>&</sup>lt;sup>1</sup> The reader is referred to the FEniCS website which provides extended documentation for the Python API along with several demos for using the software.

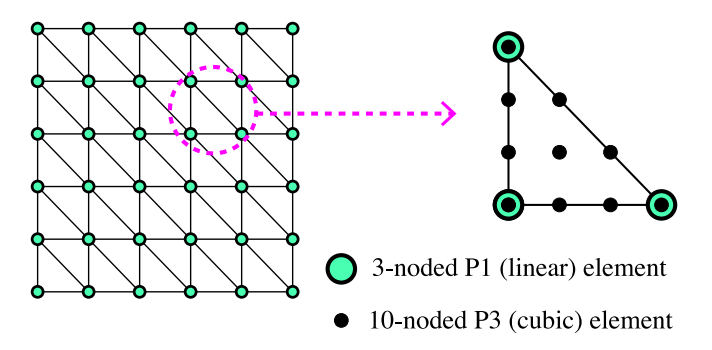


Fig. 2. Illustration of the P3-P1 mixed finite element showing the 3-noded P1 sub-element with linear shape functions and the 10-noded P3 sub-element with cubic shape functions.

element because its evolution is dictated by the Cauchy stress. While equal low-order stabilized P1–P1 elements [69–71] (also see supplementary material Section 2.1) are attractive due to their low computational cost [72], especially in three dimensions, the pressure and stress fields predicted by low-order P1–P1 elements are not as accurate as the higher-order P2–P1 or P3–P1 elements [7,8]. Another viable yet computationally cheaper alternative to P2–P1 or P3–P1 elements is the enriched MINI-element [29,41] (see supplementary material Section 2.2); however, the implementation of free-slip conditions tangential to the domain boundaries is not straightforward in FEniCS and requires the use of weak form implementations.

## Algorithm 1: Stokes flow solution scheme

At any time step n, the following is known: the nodal positions  ${}^nx_i$  (where  $i \in \{1, 2, 3\}$ ), the damage variable  ${}^nD$  at each node, and the total elapsed time  ${}^nt$ . The solution scheme for a prescribed total time  $t_{\text{total}}$  is implemented as follows:

- 1. Initialize at step n = 0:
  - (a) Supply the finite element mesh with nodal positions  ${}^{0}x_{i}$ . Define boundaries, finite element function spaces, and Dirichlet boundary conditions.
  - (b) Set initial values for time and damage:  $^{0}t = 0$  and  $^{0}D = 0$ .
  - (c) At each node, compute the nonlocal damage weights of neighboring nodes.
- 2. While  $^n t \leq t_{\text{total}}$ :
  - (a) Solve the Stokes flow equations (Eqs. 28) using Picard iterations (see Algorithm 2) on the current reference configuration  ${}^{n}\Omega$  to obtain the velocity and effective pressure solutions  ${}^{n+1}v_{i}$  and  ${}^{n+1}\widetilde{p}$ .
  - (b) Compute  ${}^{n+1}\dot{\epsilon}_{ij}$ ,  ${}^{n+1}\widetilde{\tau}_{ij}$ , and  ${}^{n+1}\widetilde{\sigma}_{ij}$  at each node belonging to the P1 elements in the mesh using Equations (30), (19), and (22) respectively.
  - (c) Compute the nonlocal damage increment  ${}^{n}\Delta D$  at each node belonging to the P1 elements using Algorithm 3.
  - (d) Move the mesh by updating nodal positions:  ${}^{n+1}x_i = {}^n \Delta u_i + {}^n x_i$ , where the displacement increment  ${}^n \Delta u_i = {}^{n+1}v_i {}^n \Delta t$ .
  - (e) Update the elapsed time:  $^{n+1}t = {}^{n}\Delta t + {}^{n}t$  and the iteration count: n = n + 1.

## 3.2. Computation of damage increment

We employ an explicit forward Euler method in conjunction with the nonlocal integral approach to compute the creep damage increment at each time step. First, the local damage rate is computed using the Cauchy stress  $^{n+1}\sigma_{ij}$  obtained from the solution of the Stokes flow problem and the prior damage  $^nD$ , as summarized in Algorithm 3. Next,

## Algorithm 2: Picard iteration scheme for Stokes flow in 2D

Let  ${n+1 \choose (m)} v_1$  and  ${n+1 \choose (m)} v_2$  denote the horizontal and vertical components of velocity, respectively, and  ${n+1 \choose (m)} \widetilde{p}$  denote the effective pressure determined on the current reference configuration  ${}^n \Omega$  at Picard iteration m. The Picard iteration scheme is implemented as follows:

- 1. Initialize the velocity and pressure variables at iteration m = 0:
  - (a) Set  $_{(0)}^{n+1}v_1 = {}^nv_1$  and  $_{(0)}^{n+1}v_2 = {}^nv_2$  everywhere in the domain.
  - (b) Set  ${n+1 \choose 0} \widetilde{p} = {n \choose p}$  everywhere in the domain.
- 2. Initialize the maximum relative error  $\varepsilon$  to be greater than the chosen tolerance  $\varepsilon_{\text{tol}}$ .
- 3. While  $\varepsilon > \varepsilon_{\text{tol}}$ :
  - (a) Compute the nonlinear viscosity  $\eta \binom{n+1}{(m)} \mathbf{v} = \frac{1}{2} B \left( \binom{n+1}{(m)} \dot{\boldsymbol{\epsilon}}^{\text{eq}} \right]^2 + \gamma \right)^{\frac{1-N}{2N}}$  for iteration m using  $\binom{n+1}{(m)} v_1, \binom{n+1}{(m)} v_2$ .
  - (b) Solve the Stokes flow equations (Eqs. 28) with the viscosity  $\eta \binom{n+1}{(m)} v$  to obtain  $\binom{n+1}{(m+1)} v_1$ ,  $\binom{n+1}{(m+1)} v_2$ , and  $\binom{n+1}{(m+1)} \widetilde{p}$ . This is done in FEniCS software by using the solve() function.
  - $\text{(c) Calculate relative $L^2$ error norms: $\varepsilon_1 = \frac{||_{(m+1)}^{n+1} v_1 _{(m)}^{n+1} v_1||}{||_{(m+1)}^{n+1} v_1||}, $\varepsilon_2 = \frac{||_{(m+1)}^{n+1} v_2 _{(m)}^{n+1} v_2||}{||_{(m+1)}^{n+1} v_2||}, $\varepsilon_p = \frac{||_{(m+1)}^{n+1} \widetilde{p} _{(m)}^{n+1} \widetilde{p}||}{||_{(m+1)}^{n+1} \widetilde{p}||}.$
  - (d) Determine the maximum relative error:  $\varepsilon = \max\{\varepsilon_1, \varepsilon_2, \varepsilon_p\}$ .
  - (e) Update the iteration count: m = m + 1.
- 4. Upon convergence:  ${}^{n+1}v_1 = {}^{n+1}_{(m+1)}v_1$ ,  ${}^{n+1}v_2 = {}^{n+1}_{(m+1)}v_2$ , and  ${}^{n+1}\widetilde{p} = {}^{n+1}_{(m+1)}\widetilde{p}$ .

the nonlocal damage increment  ${}^n \Delta D$  is calculated using the local damage increments  ${}^n \Delta D^{\text{loc}} = {}^n \dot{D}^{\text{loc}} {}^n \Delta t$  as given by the weighted summation

$${}^{n}\Delta D\left({}^{n}\mathbf{x}\right) = \frac{\sum_{j=1}^{N^{\text{pts}}} \Phi\left({}^{0}\mathbf{x} - {}^{0}\hat{\mathbf{x}}_{j}\right){}^{n}\Delta D^{\text{loc}}\left({}^{n}\hat{\mathbf{x}}_{j}\right)}{\sum_{j=1}^{N^{\text{pts}}} \Phi\left({}^{0}\mathbf{x} - {}^{0}\hat{\mathbf{x}}_{j}\right)},\tag{31}$$

where  ${}^n \Delta t$  is a chosen time increment that ensures stability of the explicit update, and N<sup>pts</sup> is the number of material points (i.e., finite element nodes)  ${}^0 \hat{x}_j$  that neighbor  ${}^0 x$ , that is, the number of points satisfying  $\|{}^0 x - {}^0 \hat{x}_j\| \le l_c$ . The nonlocal weights  $\Phi \left( {}^0 x - {}^0 \hat{x}_j \right)$  are calculated and stored in a Python dictionary at the beginning of the simulation, instead of recalculating the weights at every time step. Finally, the damage variable in the updated configuration is computed as

$$^{n+1}D = ^nD + ^n\Delta D. \tag{32}$$

**Remark 9.** To reduce the computational burden, we only compute the nonlocal damage weights at the beginning of the simulation using materials points  ${}^{0}x$  over the initial reference configuration. Considering that the spatial locations of material points and their relative distances change as the domain deforms, it may be necessary to periodically recalculate the nonlocal weights, especially over time scales associated with large displacements.

As an alternative to the weighted summation in Eq. (31), the nonlocal damage increment can be obtained using the implicit gradient formulation presented in Section 2.4.2. The nonlocal damage rate  ${}^{n}\dot{D}$  is computed by taking the finite

element discretization of Eq. (16), whose variational form is obtained by introducing a test function z, integrating by parts, and then applying Gauss's theorem. The variational form over the current reference configuration  ${}^{n}\Omega$  is stated as follows:

Find  ${}^{n}\dot{D} \in \mathcal{Z}$ , such that  $\forall z \in \mathcal{Z}$ :

$$\int_{n\Omega} z^{n} \dot{D} d\Omega + \frac{l_{c}^{2}}{4\kappa} \int_{n\Omega} \frac{\partial z}{\partial n_{x_{i}}} \frac{\partial^{n} \dot{D}}{\partial n_{x_{i}}} d\Omega - \int_{n\Omega} z^{n} \dot{D}^{loc} d\Omega = 0$$
 and so 
$$= 0$$
 on 
$$= 0$$
 (33)

where  $\mathcal{Z}$  is an appropriate scalar function space, and the local damage rate  ${}^n\dot{D}^{\mathrm{loc}}$  is computed from Eq. (8) at a given material point. The above equation is discretized using linear P1 interpolants and evaluated using the FEniCS solve() function with zero flux conditions on all external boundaries. After solving for  ${}^n\dot{D}$ , the nonlocal damage increment is calculated as  ${}^n\Delta D = {}^n\dot{D}$   ${}^n\Delta t$  for an appropriately chosen time increment  ${}^n\Delta t$ . The major advantage of the implicit gradient formulation is that nonlocal damage will always be computed over the current reference configuration  ${}^n\Omega$  without needing to determine the updated nonlocal weights at each time step.

The simulation of creep fracture using either the integral or gradient nonlocal approaches can be quite challenging, requiring us to employ several numerical controls in order to continue computation over long times, as discussed below:

- 1. We restrict the value of the damage variable  $D \in [0,1)$  by a maximum value  $D^{\max} = 0.97$  or 0.999 in order to avoid a rank deficient tangent (stiffness) matrix. The physical implication of setting  $D^{\max} < 1$  is that the fully damaged regions still possess a small residual strength, which can lead to unphysical stress redistribution. To correct this discrepancy, an element removal scheme can be implemented to remove failed elements from the finite element mesh; however, this is only valid if the damage zone represents void space due to crack opening. The element removal scheme can be implemented as follows: before proceeding from time step n to n+1, we search for elements where n+1 n+1
- 2. Experimental and modeling studies on creep damage in ice indicate an abrupt failure (rupture) as accumulated damage D becomes greater than 0.6 [20]. To account for this behavior, a critical damage parameter  $D^{cr} = 0.6$  is introduced so that as soon as  $D \ge D^{cr}$  we can immediately set damage to a maximum value  $D^{max}$  and damage rate  $\dot{D}^{loc} = 0$ . Although introducing the  $D^{cr}$  parameter into the damage model improves the numerical convergence in Abaqus software using the Maxwell viscoelastic model, it does not affect either the convergence of the FEniCS software using the viscous Stokes model or the crevasse growth results in any significant way.
- 3. Because we employ the explicit forward Euler method to update damage in time, it is essential that we determine a stable time increment  ${}^n\Delta t$  to compute  ${}^n\Delta D$  according to Eq. (32) to obtain an accurate solution. To determine an appropriate time increment, we impose the condition  $\Delta D^{\rm loc} \leq 0.05$  at every material point and then calculate  ${}^n\Delta t$  as

$$^{n}\Delta t = \frac{\max(^{n}\Delta D^{\text{loc}})}{\max(^{n}\dot{D}^{\text{loc}})},\tag{34}$$

where  $\max(^n\dot{D}^{\rm loc})=0.05$  is the maximum of the local damage rates at all the material points in the domain. A consequence of the above strategy is that it prevents excessively fast growth of damage before it reaches critical damage, which minimizes changes in the damage state between  $^{n+1}\Omega$  and  $^n\Omega$  and thus alleviates numerical difficulties related to time stepping. Initially, when damage is low, the damage rate  $^n\dot{D}^{\rm loc}$  is small and so the time step  $^n\Delta t$  calculated from Eq. (34) is large. Because we use an explicit scheme to update (or move) the mesh at every time step, we impose a maximum time step of two hours; this ensures that the displacement of material points between  $^{n+1}\Omega$  and  $^n\Omega$  is sufficiently small so that the approximation in Eq. (30) remains valid. As damage accumulates the local damage rate  $^n\dot{D}^{\rm loc}$  increases, thus causing the time step to gradually decline, with the smallest time step size reaching as low as 5 s close to rupture.

## Algorithm 3: Numerical implementation of nonlocal damage

The local damage increment  ${}^n \Delta D^{\text{loc}}$  is computed during time step n based on the currently existing damage  ${}^n D$  and effective Cauchy stress  ${}^{n+1} \widetilde{\sigma}_{ij}$ . The nonlocal damage increment  ${}^n \Delta D$  is then computed as a weighted summation through the following steps:

- 1. Compute the local damage rate  ${}^{n}\dot{D}^{loc}$  throughout the domain. At every finite element node:
  - (a) Compute the effective max principal stress  $^{n+1}\widetilde{\sigma}^{(I)}$ , von Mises stress  $^{n+1}\widetilde{\sigma}^{v}$ , and first stress invariant  $^{n+1}\widetilde{\sigma}_{kk}$ .
  - (b) Compute the Hayhurst stress  $^{n+1}\chi$ .
  - (c) Compute the damage evolution:  $f = \hat{B} \frac{\langle {}^{n+1}\chi \rangle^r}{(1-nD)^{k\sigma}}$ , where  $k_{\sigma} = k_1 + k_2|^{n+1}\sigma_{kk}|$ .
  - (d) To allow only tensile damage, we enforce the condition that  ${}^{n}\dot{D}^{loc} = f$  if  ${}^{n+1}\sigma_{kk} \ge 0$  and  ${}^{n}\dot{D}^{loc} = 0$  otherwise.
  - (e) If  ${}^nD = D^{\max}$  then  ${}^n\dot{D}^{\text{loc}} = 0$ .
- 2. Compute the time step:

$$^{n}\Delta t = \min\left(\frac{0.05}{\max(^{n}\dot{D}^{\mathrm{loc}})}, 2 \text{ hrs}\right).$$

- 3. Compute the local damage increment  ${}^{n}\Delta D^{\text{loc}} = {}^{n}\dot{D}^{\text{loc}} {}^{n}\Delta t$  at each node.
- 4. Compute the nonlocal damage increment  ${}^{n}\Delta D$  at each node using the integral approach (Eq. 31) or the implicit gradient approach (Eq. 33).
- 5. Update damage at each node:  $^{n+1}D = {}^{n}D + {}^{n}\Delta D$ .

## 4. Numerical examples

In this section, we first verify the Picard iteration based nonlinear solver for the Stokes model by performing a verification study against a manufactured analytical solution [10,73]. This verification study is repeated using the Newton's method in the supplementary material Section 3. Following that, we establish the viability of the updated-Lagrangian formulation by simulating constant velocity and gravity-driven creep flow in idealized rectangular ice slabs and comparing the results with those obtained using the total Lagrangian formulation based on the Maxwell viscoelastic rheological model, previously established by Duddu et al. [20–23]. As noted earlier, the Stokes flow formulation is evaluated using the open-source finite element software FEniCS using triangular meshes, whereas the viscoelastic formulation is solved using commercial finite element software Abaqus using quadrilateral meshes. First, we benchmark the rheological models using idealized rectangular domains under simple loading conditions. Second, we introduce a notch in the rectangular domain at mid-length to determine the effects of stress concentrations (or singularities). Third, we incorporate the creep damage law detailed in Section 2.4 in order to simulate damage (crevasse) propagation. All simulations are performed in two dimensions assuming plane strain conditions on a rectangular slab of ice 500 m  $\times$  125 m (length L  $\times$  height H) as shown in Fig. 3. Boundary conditions (rollers) are specified in all simulations to constrain vertical displacement on the bottom edge of the domain and horizontal displacement on the left edge, thus allowing free slip. The isotropic material properties of ice at the temperature -10 °C are given in Table 2. Thus, in this article, we only consider idealized rectangular geometries and boundary conditions and assume that the temperature is constant throughout the ice slab to conduct proof-of-concept studies that are still relevant for understanding crevasse propagation in glaciers and land ice sheets. Such domain geometries are commonly used to conduct fundamental studies to investigate the conditions that enable fracture in ice bodies and provide insights into the mechanisms behind iceberg calving [18,19,74,75]. More realistic and complex geometries, loading, and boundary conditions shall be considered in a future paper focused on the simulation of ice sheet evolution.

Table 3 Numerical verification study of the nonlinear Stokes model using Picard iteration scheme. The  $L^2$  error norms  $\varepsilon_{\nu}$  and  $\varepsilon_p$  for velocity magnitude and pressure, respectively, given in Eq. (36) are presented for different mesh sizes.

Mesh	#DoF	$\varepsilon_{\pmb{v}}$	Rate	$\varepsilon_p$	Rate
$4 \times 4$	187	6.96e-4	_	1.04e-1	_
$8 \times 8$	659	5.97e-5	3.54	1.54e-2	2.75
$16 \times 16$	2467	5.11e-6	3.55	1.96e - 3	2.98
$32 \times 32$	9539	3.47e-7	3.88	2.68e-4	2.87

## 4.1. Numerical verification study

In this section we verify our implementation of the Stokes rheological model by demonstrating that numerical results converge to a known analytical solution with progressive mesh refinement. A previous study in [76] used linear Stokes rheology (i.e., with constant viscosity) and verified the FEniCS software for Poiseuille flow and several other gravity-driven flow benchmark examples that have exact solutions. On the verification of Stokes ice-sheet models using manufactured solutions we refer the reader to [8]. Herein, we conduct one such verification study to show that the *nonlinear* Stokes formulation converges to the manufactured solution presented in [10,73] for incompressible flow, which is given by

$$v_1^* = x_1 + x_1^2 - 2x_1x_2 + x_1^3 - 3x_1x_2^2 + x_1^2x_2,$$

$$v_2^* = -x_2 - 2x_1x_2 + x_2^2 - 3x_1^2x_2 + x_2^3 - x_1x_2^2,$$

$$p^* = x_1x_2 + x_1 + x_2 + x_1^3x_2^2 - 4/3,$$
(35)

on the unit square domain  $\Omega = [0, 1] \times [0, 1]$ . In this example we ignore damage and take  $\eta(v) = ([\dot{\epsilon}^{eq}]^2 + \gamma)^{\frac{1-N}{2N}}$ , where  $\dot{\epsilon}^{eq}$  is defined in Eq. (20). The force terms  $b_i$  are chosen to satisfy the momentum balance equation after substituting in the solutions  $v_1^*$ ,  $v_2^*$ , and  $p^*$ , as given in [77]. Dirichlet boundary conditions on velocity are obtained by applying Eq. (35) along domain edges. In order to compare with the numerical study conducted in Section 3.3 of [10], we employ P2-P1 (Taylor-Hood) elements and take the viscosity parameter N=3.5. Starting with a 4 × 4 structured mesh over the unit domain  $\Omega$ , we progressively refine the mesh by reducing the element size by half. For each mesh size we compute the  $L^2$  error norms,

$$\varepsilon_{\mathbf{v}} = \sqrt{\frac{\sum_{k=1}^{N^{P2}} (\|\mathbf{v}\|_{k} - \|\mathbf{v}^{*}\|_{k})^{2}}{\sum_{k=1}^{N^{P2}} (\|\mathbf{v}^{*}\|_{k})^{2}}}, \quad \varepsilon_{p} = \sqrt{\frac{\sum_{k=1}^{N^{P1}} (p_{k} - p_{k}^{*})^{2}}{\sum_{k=1}^{N^{P1}} (p_{k}^{*})^{2}}},$$
(36)

for velocity magnitude and pressure, respectively, which are reported in Table 3. In the above equations,  $N^{P1}$  and  $N^{P2}$  are the number of nodes in the P1 and P2 spaces, respectively; and  $\|\mathbf{v}\|_k$  and  $p_k$  are the velocity magnitude and pressure, respectively, at the kth node. The  $\varepsilon_{\mathbf{v}}$  and  $\varepsilon_{p}$  error norms decrease with third and second order convergence respectively, which is consistent with the results reported in [10]. A repeated study using P3–P1 elements showed similar convergence rates with smaller error norms for coarse meshes (not shown here), thus verifying the FEniCS implementation.

## 4.2. Constant velocity creep flow

In this set of benchmark studies comparing the Stokes flow and Maxwell viscoelastic models, we simulate a standard creep test by disregarding gravity and prescribing a constant, uniform velocity v = 0.5 m/day on the right edge of the rectangular domain, as shown in Fig. 3(a), so that the resulting strain rate of  $1.157 \times 10^{-8}$  s<sup>-1</sup> is on the order of the strain rates observed in real glaciers.

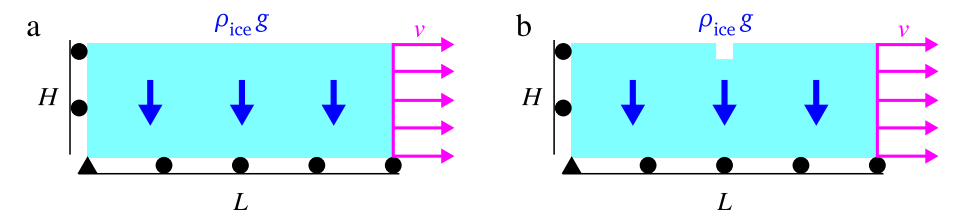


Fig. 3. Domain setup including applied velocity v and gravitational body force  $\rho_{\text{ice}g}$  with (a) no notch and (b) a 10 m × 10 m notch centered along the top surface of the slab. Domain height H=125 m, length L=500 m. The applied velocity v=0.5 m/day and body force  $\rho_{\text{ice}g}=(917 \text{ kg/m}^3 \times 9.81 \text{ m/s}^2)$ .

## 4.2.1. Glaciological stress predictions without damage

We first consider the case when damage is prescribed to be zero throughout the domain at all times. Both rheological models are simulated on structured finite element meshes with an element size h=5 m. The results of this study are presented in Fig. 4, wherein we plot the horizontal Cauchy stress  $\sigma_{11}$  predicted by each rheological model as a function of time. The viscoelastic model describes the time-dependent behavior, as shown in Fig. 4(a), wherein stress  $\sigma_{11}$  gradually plateaus at 506 kPa over a short timespan ( $t \approx 8$  h); whereas, the Stokes flow model describes the steady-state behavior, wherein the equilibrated stress  $\sigma_{11}=506$  kPa is established instantly. As shown in Fig. 4(b), the value of  $\sigma_{11}$  decays (very slightly) over time in the updated-Lagrangian formulation of Stokes flow equations, because the mesh update scheme allows for the thinning of the ice slab with time as large viscous deformations extend the slab length. If the mesh update scheme was not implemented, then stress would not decay as displayed in Fig. 4(c). Thus, this study verifies that for simple loading cases and in the absence of any damage, both the Stokes flow and Maxwell viscoelastic models describe the same constitutive behavior in the small deformation regime.

We now introduce a 10 m  $\times$  10 m notch at mid-length of the top surface of the rectangular domain, as shown in Fig. 3(b), so as to study the effects of stress concentrations. The same velocity boundary conditions are specified as before, and gravity and damage are disregarded. Both rheological models are simulated on unstructured meshes that are highly refined around the notch with an element size h=0.25 m. The field contour plot of the Hayhurst stress  $\chi$  in the notched domain at time t=12 h predicted by the Stokes model is shown in Fig. 5(a)–(b), which is in good qualitative agreement with that obtained from the viscoelastic model. In order to measure the quantitative differences between the stress fields predicted by the two rheological models, we consider the  $L^2$  and  $L^\infty$  relative error norms defined as

$$\varepsilon_{L^{2}} = \sqrt{\frac{\sum_{k=1}^{N^{IP}} \left(\chi_{k}^{\text{Abaqus}} - \chi_{k}^{\text{interp}}\right)^{2}}{\sum_{k=1}^{N_{\text{pts}}} \left(\chi_{k}^{\text{Abaqus}}\right)^{2}}},$$
(37)

$$\varepsilon_{L^{\infty}} = \frac{\max_{k} \left| \chi_{k}^{\text{Abaqus}} - \chi_{k}^{\text{interp}} \right|}{\max_{k} \left| \chi_{k}^{\text{Abaqus}} \right|},\tag{38}$$

where N<sup>IP</sup> is the number of Abaqus integration points,  $\chi_k^{\text{Abaqus}}$  is the Hayhurst stress at the kth Abaqus integration point, and  $\chi_k^{\text{interp}}$  is the Hayhurst stress interpolated from FEniCS nodes at the kth Abaqus integration point.

The relative errors  $\varepsilon_{L^2}$  and  $\varepsilon_{L^\infty}$  in Hayhurst stress  $\chi$  versus time are plotted in Fig. 5(c), wherein each measure of relative error shows a time-dependence because the stress fields predicted by the Maxwell viscoelastic model gradually increase from zero to the steady-state value, whereas in the Stokes model the steady-state stress is directly established based on the quasi-static assumption. It is evident from Fig. 5(c) that  $\varepsilon_{L^2}$  decays quickly to about 3% after t=4 h, indicating that both rheological models predict approximately the same stresses in bulk regions of the domain; whereas,  $\varepsilon_{L^\infty}$  decays to about 42%, suggesting that in the vicinity of the notch the two models predict substantially different stresses. However, this discrepancy is anticipated for at least two reasons: (1) in the Maxwell model both elastic and viscous strains are included, whereas in the Stokes model only viscous strains are considered;

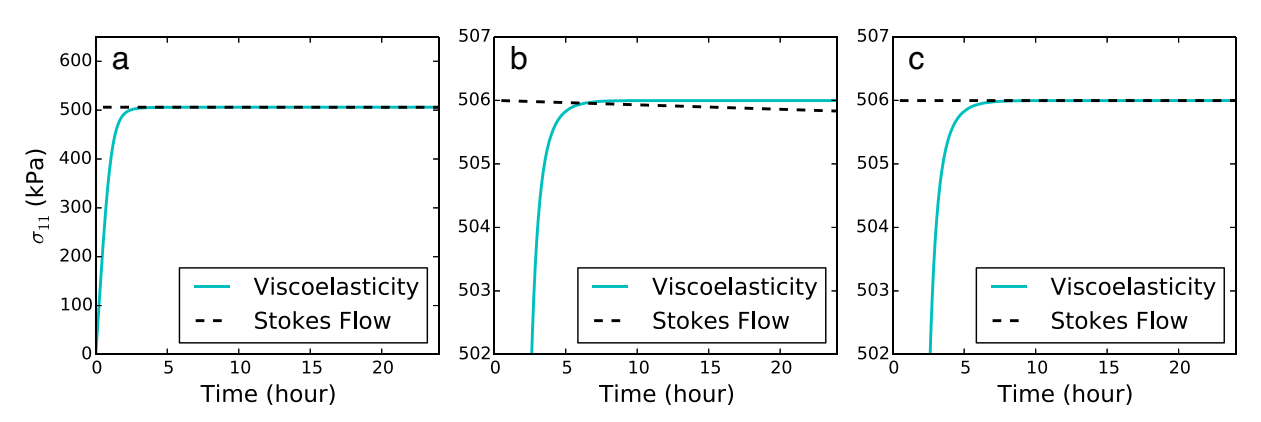


Fig. 4. Results of the uniaxial creep test with constant strain-rate (or velocity) v = 0.5 m/day showing (a) horizontal Cauchy stress  $\sigma_{11}$  vs. time. The y-axis is scaled for a closer view of (b)  $\sigma_{11}$  vs. time when using the updated-Lagrangian mesh update scheme and (c)  $\sigma_{11}$  vs. time without the mesh update scheme.

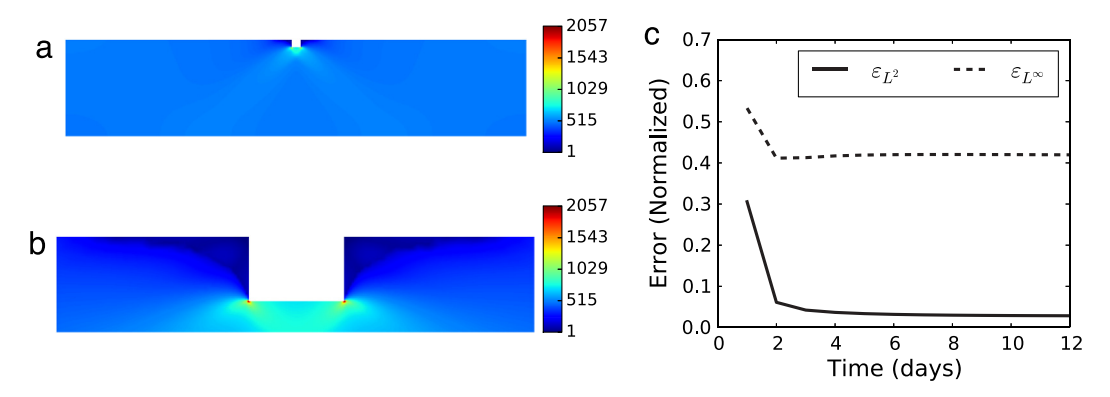


Fig. 5. Hayhurst stress  $\chi$  (in kPa) predicted by the Stokes flow rheological model for an ice slab with an applied creep velocity v=0.5 m/day after 12 h. Subfigure (a) shows  $\chi$  over the whole domain; subfigure (b) shows a zoomed-in display of  $\chi$  near the notch; and subfigure (c) displays the normalized errors  $\varepsilon_{L^2}$  and  $\varepsilon_{L^\infty}$  (given by Eqs. (37) and (38), respectively) between viscoelastic and Stokes flow solutions for  $\chi$ .

and (2) the Maxwell model considers compressible elasticity (Poisson's ratio  $\nu=0.35$ ), whereas the Stokes model enforces incompressibility. Based on this study, we suspect that the fracture behavior predicted by the two rheological models for ice would be different because the crack growth rate depends on the local differences in the Hayhurst stress, particularly in the vicinity of the notch.

#### 4.2.2. Mode I creep crack growth

In this section, we simulate and compare mode I creep fracture in ice predicted by the Maxwell viscoelastic and Stokes flow models using the nonlocal creep damage law detailed in Section 2.4. Additionally, we compare the Stokes model results obtained with and without the element removal scheme discussed in Section 3.2. We consider three metrics to compare creep fracture behavior across the different simulation studies: (1) the time required for crack tip damage initiation (i.e., when the first material point reaches  $D = D^{\max}$ ); (2) the time for full crack penetration of the slab; and (3) the geometrical differences in damage (fracture) morphologies. We use the notched domain shown in Fig. 3(b) with the same applied velocity and boundary conditions as in the previous study, and gravity is disregarded. To eliminate any discrepancies arising from the time-dependent strain evolution in the Maxwell viscoelastic model, we first allow the stresses to equilibrate by holding damage at zero for 12 h and then let damage evolve. Crack growth using both rheological models is simulated on meshes that are structured around the notch and within the entire nonlocal damage zone with an element size h = 2 m; whereas, far from the notch and damage zone the mesh is unstructured with a maximum element size h = 12.5 m. The mode I crack (damage) growth results obtained from the simulations studies are shown in Figs. 6 and 7.

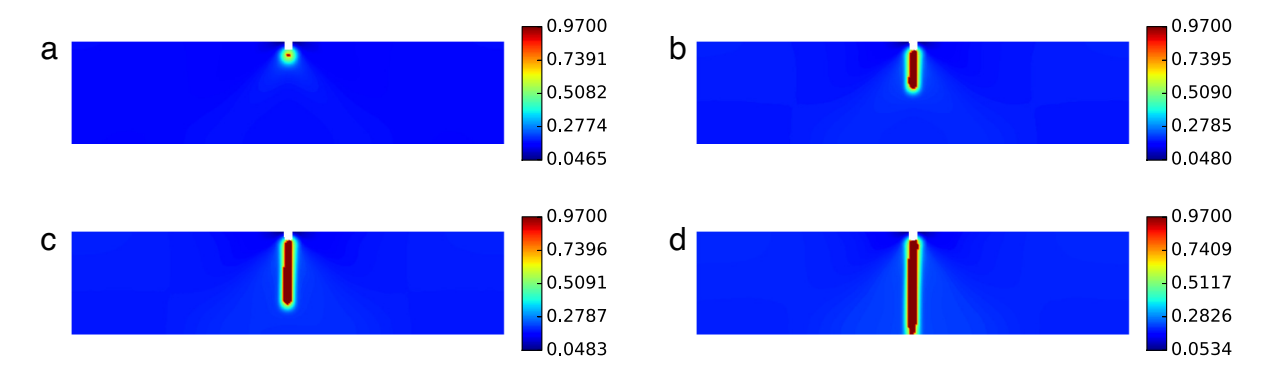


Fig. 6. Crevasse propagation predicted by the Stokes flow rheological model for an ice slab with an applied creep velocity v = 0.5 m/day. The damage variable is shown at (a) 110.789 h, (b) 119.114 h, (c) 121.876 h, and (d) 122.6 h.

Both Stokes flow and viscoelastic rheological models predict identical damage morphology, wherein the crack initiates beneath the notch and then propagates vertically towards the bottom of the ice slab; so we only show the Stokes flow result (without element removal) in Fig. 6. The crevasse depth d (measured from the damage contour plots) is normalized by the domain height H = 125 m and plotted as a function of time for each simulation in Fig. 7. The results in Fig. 7(a) indicate that the crack tip damage initiation begins at 103.4 and 110.789 h in the Maxwell viscoelastic model and Stokes flow model, respectively; thus, damage initiation occurs slightly earlier in the viscoelastic model. Fulldepth crack penetration occurs at 108.97 and 122.6 h for the viscoelastic and Stokes flow model, respectively; thus, the elapsed time between damage initiation and complete crack penetration is 5.57 and 11.811 h. These discrepancies in crack growth behavior are anticipated (based on the previous study in Section 4.2.1), because the Havhurst stress is larger at notch tip in comparison with that predicted by the Stokes model. Interestingly, we find that implementing the element removal scheme shows slight or no difference in the rate of damage growth compared with  $D^{\text{max}} = 0.97$  or 0.999. In Fig. 7(b), we compare the implicit gradient and explicit integral damage approaches. The integral approach shows better agreement with the implicit gradient approach when using the Green's function to determine the nonlocal weights, because the Green's function is a weak solution to Eq. (16) [63]. In Fig. 7(c), we compare the results from P3-P1 and P2-P1 (Taylor-hood) mixed elements with that from the stabilized P1-P1 element (see the online supplementary material Section 2.1). We find that P3–P1 and P2–P1 elements predict identical crevasse growth rates; whereas, the stabilized P1-P1 element predicts a different result because the incompressibility condition is not well enforced, and consequently the Hayhurst stress under the crack tip is different. Finally, we conduct a mesh convergence study by progressively reducing the mesh size h within the nonlocal damage zone. Fig. 7(d) illustrates that we obtain reasonably consistent crack growth rates when taking an element size h = 5, 2.5, 1.25 m, so long as it is smaller than the characteristic length scale  $l_c = 10$  m. In conclusion, this study indicates that Stokes flow and viscoelastic rheological models predict different damage initiation times and crack growth rates; however, it is important to note that the constant velocity creep flow is not representative of glacier deformation occurring due to gravity-induced flow.

#### 4.3. Gravity-driven creep flow

For this next set of benchmark studies comparing the Stokes flow and Maxwell viscoelastic models, we simulate the gravity-driven creep test, wherein the rectangular slab of ice is deforming only due to its own self-weight, as shown in Fig. 3(a), without any applied velocity at the right edge. Gravity loading is applied as a body force  $b_2 = -\rho_{ice}g$  in the vertical dimension, where  $\rho_{ice}$  is the density of ice given in Table 2 and g is gravitational acceleration.

#### 4.3.1. Glaciological stress predictions without damage

We first consider the case when damage is prescribed to be zero throughout the domain at all times. Both rheological models are simulated on unstructured meshes that are generated by specifying element sizes h=10 m and h=2 m on the left and right domain edges, respectively. We use a finer mesh resolution near the right edge (representing the glacier terminus) in order to accurately capture the stresses induced by warping (distortion). The contour plots of the horizontal Cauchy stress  $\sigma_{11}$  and stress invariants predicted by Stokes model are shown in Fig. 8. Near the left edge of the domain the horizontal Cauchy stress  $\sigma_{11}$  is uniform in the horizontal direction with tension on the top and

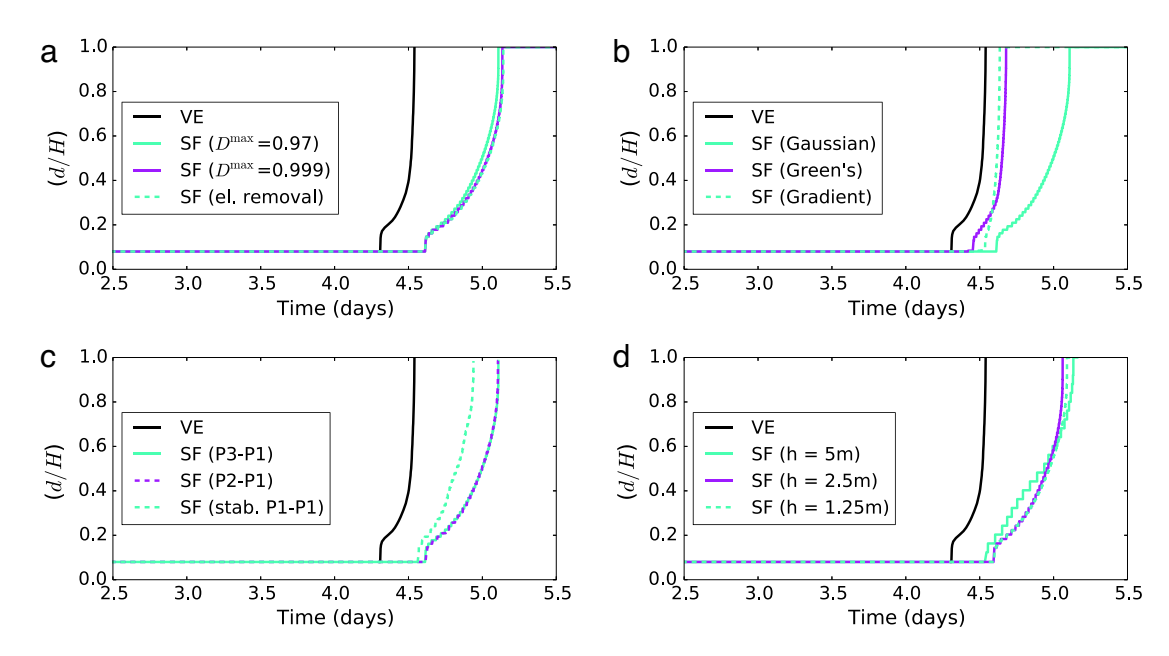


Fig. 7. Crevasse depth (d) normalized with the domain height (H = 125 m) through an ice slab undergoing constant velocity creep flow, plotted as a function of time from 2.5 to 5.5 days. The abbreviations VE and SF refer to the viscoelastic and Stokes flow rheological models, respectively. Subfigure (a) shows a parametric study of  $D^{\text{max}}$  in order to compare between continuum damage and the element removal scheme. (Note that in all simulations we set  $D^{\text{max}} = 0.97$ , except for the magenta line Subfigure (a).) Subfigure (b) shows crevasse growth rates for the nonlocal integral using separate weighting functions (Gaussian and Green's function) and the implicit gradient damage scheme. Subfigure (c) shows the crevasse growth rate for different orders of interpolation for the velocity solution. Subfigure (d) presents a mesh size study wherein the element size h is progressively reduced in the nonlocal damage zone.

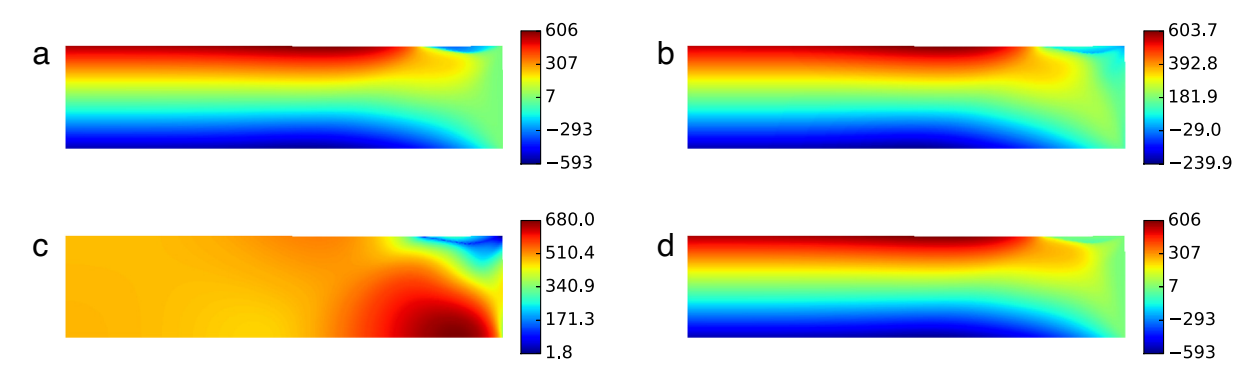


Fig. 8. Stresses predicted by the Stokes flow rheological model for an ice slab under gravitational loading after 5 days. The stress components are: (a) horizontal Cauchy stress  $\sigma_{11}$ ; (b) Hayhurst stress  $\chi$ ; (c) the von Mises stress  $\sigma^{v}$ ; and (d) the max principal stress  $\sigma^{(I)}$ . All units are in kPa.

compression at the bottom and is qualitatively similar to the Hayhurst stress  $\chi$  and the max principal stress  $\sigma^{(I)}$ , as evident from Fig. 8; however, near the right edge the normal stress  $\sigma_{11}$  is much smaller and the shear stress  $\sigma_{12}$  much larger than elsewhere in the domain, as reflected in the von Mises stress plots in Fig. 8(c). These large shear stresses near the right edge cause warping and even small compressive stresses at the upper-right corner. All the contour plots of stress and its invariants predicted from the Maxwell viscoelastic model look very similar to those predicted by the Stokes model, so they are not shown here.

To measure the quantitative differences between the Stokes flow and Maxwell viscoelastic models, we consider two metrics: (1) errors (differences to be precise) in stress fields and their time evolution; and (2) time evolution of the displacement at the right edge of the domain (signifying the glacier terminus). We plot the relative error norms  $\varepsilon_{L^2}$  and  $\varepsilon_{L^\infty}$  defined in Eqs. (37) and (38), respectively, for the Hayhurst stress  $\chi$  versus time in Figs. 9(a) and 9(c) over the short and long timescales, respectively. The two error measures show a time dependency due to the differences

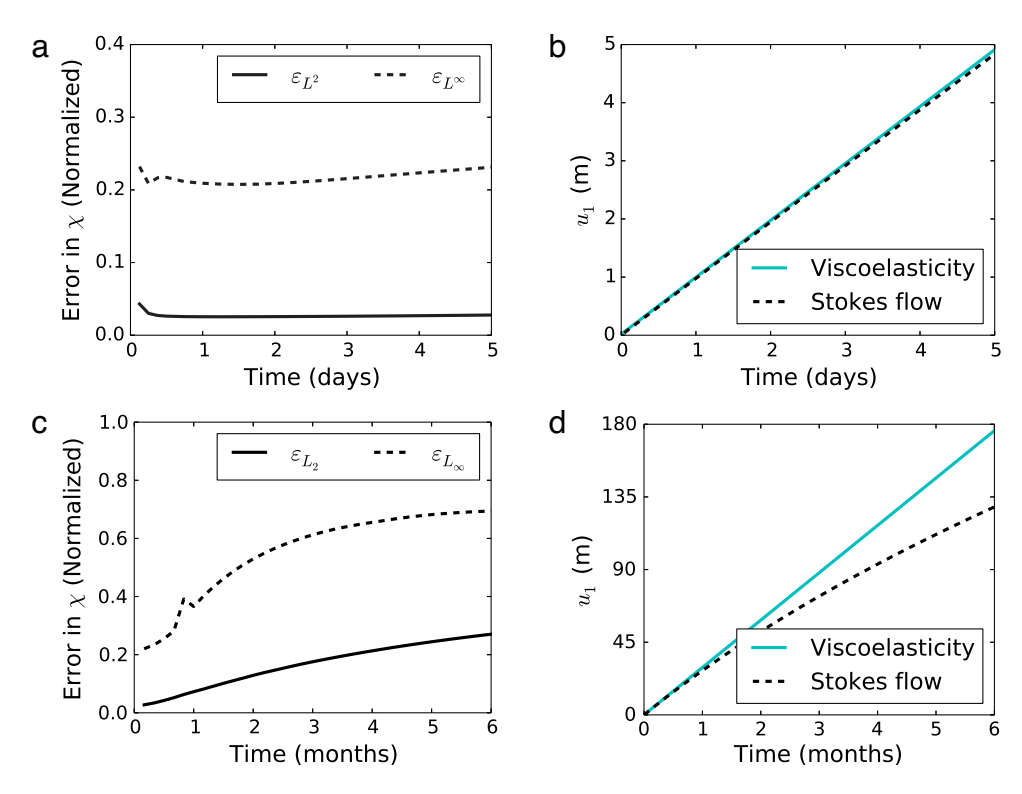


Fig. 9. Viscoelastic and Stokes flow model predictions for gravity-driven creep flow. Subfigures (a) and (c) show the normalized errors  $\varepsilon_{L^2}$  and  $\varepsilon_{L^\infty}$  (given by Eqs. (37) and (38), respectively) between viscoelastic and Stokes flow results for the Hayhurst stress  $\chi$ . Subfigures (b) and (d) show the maximum horizontal displacement  $u_1$  of the ice slab from both models.

in the Maxwell viscoelastic and the viscous Stokes models, as explained in Section 4.2.1. Over the short timescale (i.e., up till five days), the  $\varepsilon_{L^2}$  error is consistently low (<3%), indicating good agreement between the two rheological models in the bulk domain; however,  $\varepsilon_{L^\infty}$  is substantially high ( $\approx$ 23%) and mainly arises from the discrepancies in stress distribution at locations near the upper-right corner of the domain. Over the long timescale (i.e., after 6 months),  $\varepsilon_{L^2}$  and  $\varepsilon_{L^\infty}$  gradually increase to 27% and 70%, respectively; this happens because the stress predicted (under gravity loading) by the updated-Lagrangian Stokes flow formulation will slowly decay over time as the geometry of the slab changes (i.e., the slabs become thinner in the vertical direction, which reduces the over-burden pressure at the glacier bottom). The maximum creep displacement of the ice slab predicted by the viscoelastic and Stokes models, plotted in Figs. 9(b) and 9(d), shows excellent agreement during the first five days; however, after several months the Stokes model predicts a slower rate of creep flow. This study illustrates that in idealized rectangular glaciers without defects or notches both rheological models describe the same constitutive behavior (similar stress fields and maximum creep displacement) only over the short timescale, even though  $\varepsilon_{L^\infty}$  in stress fields is considerably large near the right edge (terminus). In conclusion, the long time behavior predicted by the updated-Lagrangian Stokes formulation is more physical than that predicted by the total Lagrangian viscoelastic model.

We now consider a 10 m  $\times$  10 m notch at mid-length of the top surface of the rectangular domain subjected to gravity-driven creep flow, as shown in Fig. 3(b), so as to study the effects of stress concentrations. Both rheological models are simulated on unstructured meshes that are highly refined around the notch with an element size h=0.25 m. The field contour plot of the Hayhurst stress  $\chi$  in the notched domain at time t=12 h predicted by the Stokes model is shown in Fig. 10(a)–(b), which is in good qualitative agreement with that obtained from the viscoelastic model. The notch corners introduce stress concentrations (singularities, to be precise), as evident form Fig. 10(b). The relative errors  $\varepsilon_{L^2}$  and  $\varepsilon_{L^\infty}$  for the Hayhurst stress  $\chi$  as defined in Eqs. (37) and (38), respectively, are shown in Fig. 10(c). While the  $\varepsilon_{L^2}$  error is consistently low (<5% for t>4 h),  $\varepsilon_{L^\infty}$  is substantially large ( $\approx$ 42%); this discrepancy arises not only from differences in the magnitude, but also in the spatial distribution of stress around the notch corners. An important detail to note is that we use an extremely fine mesh resolution (h=0.25 m) to compare the stresses near the

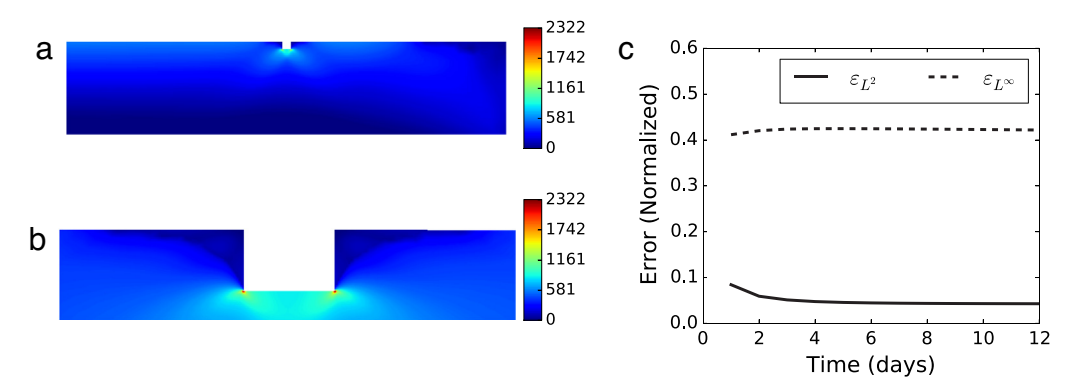


Fig. 10. Hayhurst stress  $\chi$  (in kPa) predicted by the Stokes flow rheological model for an ice slab under gravitational loading after 12 h. Subfigure (a) shows  $\chi$  over the whole domain; subfigure (b) a zoomed-in display of  $\chi$  near the notch; and subfigure (c) displays the normalized errors  $\varepsilon_{L^2}$  and  $\varepsilon_{L^\infty}$  between viscoelastic and Stokes flow solutions for  $\chi$ .

notch tip, whereas during damage growth simulations we take the mesh resolution to be reasonably coarse (h = 2 m). However, we observed the same trends in  $\varepsilon_{L^2}$  and  $\varepsilon_{L^{\infty}}$  even in the coarser meshes.

## 4.3.2. Crevasse propagation under gravity-driven creep flow

We now simulate crevasse propagation in an idealized rectangular glacier under gravitational loading by employing the nonlocal continuum damage law presented in Section 2.4 in conjunction with the viscoelastic and Stokes flow rheological models. In all the following simulations, we disregarded the body force due to self-weight of ice in fully damaged zones by incorporating Eq. (24) into the Stokes equations, which allows us to perform the simulations for the entire duration of crevasse propagation without excessive mesh distortion. Through numerical studies, we demonstrate that incorporating  $\psi(D)$  is equivalent to implementing the element removal procedure discussed in Section 3.2. As before, we consider three metrics for comparing fracture behavior across the different simulation studies: (1) the time required for crack tip damage initiation (i.e., when the first material point reaches  $D = D^{\text{max}}$ ); (2) the time for full crack penetration of the slab; and (3) the geometrical differences in damage (fracture) morphologies. We use the notched domain shown in Fig. 3(b) with the same boundary conditions as specified previously for gravitydriven creep flow. To eliminate any discrepancies arising from the time-dependent strain evolution in the Maxwell viscoelastic model, we first allow the stresses to reach steady-state by holding damage at zero for 12 h and then letting damage evolve. Crack growth in both rheological models is simulated on coarser meshes that are structured around the notch and within the entire nonlocal damage zone with an element size h=2 m; whereas, far from the notch and the damage zone the mesh is unstructured with a maximum element size h = 12.5 m. A mesh size study is also performed by varying the element size h within the nonlocal damage zone to demonstrate that the formulation predicts the same crevasse growth, so long as h is smaller than the nonlocal characteristic length scale  $I_c$ .

The crevasse growth results obtained from the simulation studies are shown in Figs. 11 and 12. Both Stokes flow (with and without element removal) and viscoelastic rheological models predict identical damage morphology, wherein the crack initiates beneath the notch and then propagates vertically towards the bottom of the ice slab; so we only show the Stokes flow result (without element removal) as shown in Fig. 11. The crevasse depth d is normalized by the domain height H=125 m and plotted as a function of time for each simulation in Fig. 12. These results indicate that the crack tip damage initiation begins at 107.5 and 112.528 h in the Maxwell viscoelastic model and Stokes flow model, respectively. The Stokes flow model using the updated-Lagrangian Stokes formulation predicts that the crevasse penetrates 69% of the ice slab depth without element removal; whereas, the total Lagrangian Maxwell viscoelastic formulation predicts that the crevasse penetrates 72% of the slab depth. From Fig. 12(a), it is apparent that the damage control strategy with  $D^{\text{max}}=0.999$  gives consistent results compared to the element removal scheme, wherein the crevasse penetrates to 79% of the slab depth. Fig. 12(b) indicates that the implicit gradient damage approach predicts faster crack tip damage initiation and crevasse growth rate; although, it predicts the same final crevasse depth as the nonlocal integral approach. However, if we consider a Green's function based weighting function, the explicit integral approach shows excellent agreement with the implicit gradient approach, because the Green's function is a weak solution to Eq. (16) [63]. In Fig. 12(c), we plot the crevasse depth versus time predicted

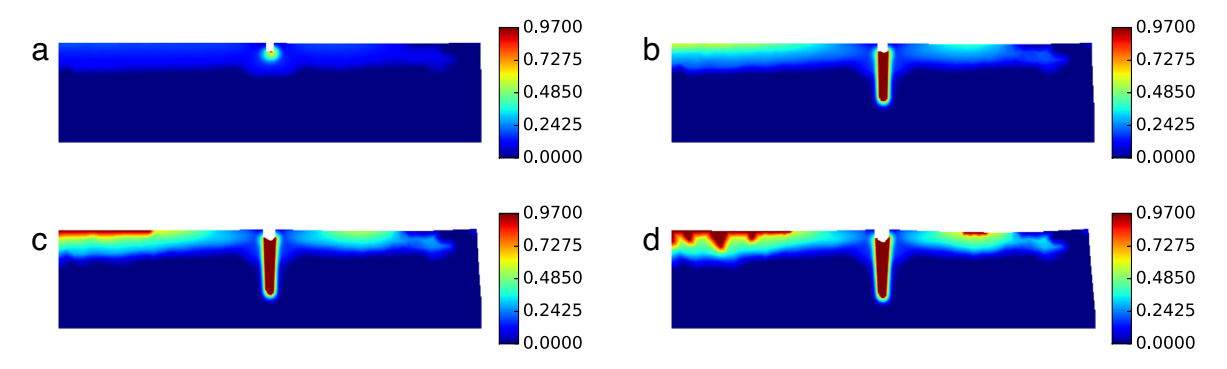


Fig. 11. Crevasse propagation predicted by the Stokes flow rheological model for an ice slab under gravitational loading. The damage variable is shown at (a) crack tip damage initiation at 112.528 h, (b) 10 days, (c) 15 days, and (d) 20 days.

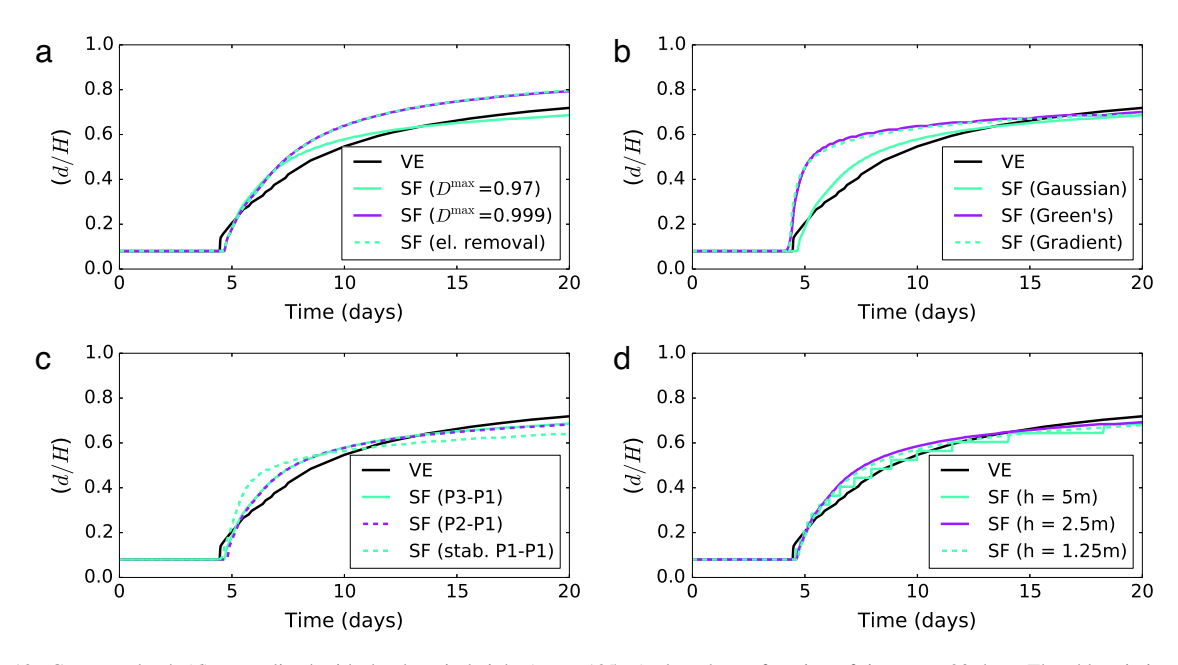


Fig. 12. Crevasse depth (d) normalized with the domain height (H = 125 m) plotted as a function of time over 20 days. The abbreviations VE and SF refer to the viscoelastic and Stokes flow rheological models, respectively. Subfigure (a) shows a parametric study of  $D^{\text{max}}$  in order to compare between continuum damage and the element removal scheme. (Note that in all simulations we set  $D^{\text{max}} = 0.97$ , except for the magenta line Subfigure (a).) Subfigure (b) shows crevasse growth rates for the nonlocal integral using separate weighting functions (Gaussian and Green's function) and the implicit gradient damage scheme. Subfigure (c) shows the crevasse growth rate for different orders of interpolation for the velocity solution. Subfigure (d) presents a mesh size study wherein the element size h is progressively reduced in the nonlocal damage zone. (For interpretation of the references to colour in this figure legend, the reader is referred to the web version of this article.)

by different order finite element approximations, including the commonly used P2–P1 (Taylor–Hood) element and a stabilized P1–P1 element (see the online supplementary material Section 2.1). The P3–P1 and P2–P1 elements yield consistent results; whereas, the stabilized P1–P1 element predicts a different crack growth rate and final crevasse depth. This occurs because the stabilized P1–P1 does not well enforce the incompressibility constraint, which affects the Hayhurst stress around the crack tip. Finally, in Fig. 12(d) we perform a mesh size study by progressively reducing the mesh size in the damage zone. Results indicate that the formulation predicts consistent damage evolution when taking an element size h = 5, 2.5, 1.25 m smaller than the characteristic length scale  $l_c = 10$  m. Based on this study we arrive at the conclusion that the Stokes flow formulation is more appropriate than the viscoelastic formulation, because while both predict the same equilibrium crevasse depth over short time scales (3.4% difference is insignificant from glaciological standpoint), the former approach is more accurate over long timescales as it accounts for large deformation induced geometry changes.

#### 4.4. Discussion

The important observations and findings of this study are summarized below:

- 1. The gravity-driven flow is a varying body-force-controlled experiment, whereas the constant velocity creep flow is a displacement-controlled experiment; consequently we observe different crack growth behavior in both experiments, as evident from Figs. 7 and 12. The constant velocity creep flow is a good benchmark test to study the differences between Stokes and viscoelastic models, although it has little physical relevance to glacier and ice sheet flow.
- 2. Under gravity-driven flow, as damage begins to accumulate under the notch, the stress is redistributed within the damage zone; consequently, the crevasse growth rate curves from both Stokes and viscoelastic model predictions are in reasonably close agreement, with less than 3.4% error in final crevasse depths over shorter timescales. Noting that the final crevasse depth is a critical factor indicative of the stability of ice sheets, we can conclude that one may neglect the contribution of elastic (stress concentration) effects and only account for nonlinear viscous flow to simulate crevasse propagation.
- 3. Under gravity-driven flow, surface crevasses do not propagate the full depth of the slab (i.e., normalized crevasse depth d/H < 1 after 20 days), unlike under constant velocity creep flow (d/H = 1 after 5 days); this is because the Hayhurst stress near the crack tip decreases as the crack grows longer. From our simulations, we observe that as the crevasse penetrates deeper the velocity gradients across the depth become smaller, leading to the progressive reduction in glaciological stress and crack growth rate with time. Thus, surface crevasse propagation under dry conditions (i.e., no hydraulic fracture) remains a quasi-static process, especially during the final stages, wherein the crevasse depth reaches its final (steady-state) depth, as evident from Fig. 12. Therefore, inertial terms need not be included in the current quasi-static fracture simulation study.
- 4. The value of the damage parameter  $\hat{B}$  in Table 1 was calibrated from experiments on laboratory grown virgin ice using the Maxwell viscoelastic model in [20], which may be an order of magnitude larger than that corresponding to glacier ice. In our recent work [23], we show that the value  $\hat{B}$  only affects crevasse growth rate but not the final (steady-state) crevasse depth; therefore, the conclusions related to surface crevasse depths and the stability of ice sheets remain valid.
- 5. From Fig. 9, it is evident that the Stokes and viscoelastic models predict different physical behavior as large deformations accrue over longer time scales, and the updated-Lagrangian formulation accounting for domain geometry changes is more appropriate than the total Lagrangian formulation. However, in order to conduct a physically accurate ice sheet flow and fracture simulation over long decadal time scales, one needs to account for mass inflow and outflow along with crack propagation and healing, which will be considered in our future research.

The overall conclusion of this study is that the updated-Lagrangian Stokes formulation is appropriate for studying gravity-flow induced glacier deformation and fracture even over short time scales, despite ignoring the elastic stress concentration effects. Furthermore, over long decadal timescales the proposed formulation would be more appropriate as it accounts for the geometry changes of the domain, when large deformations accrue over time.

### 5. Conclusion

We developed an updated-Lagrangian mixed finite element formulation based on the nonlinear Stokes flow equations and a nonlocal creep damage law to simulate crevasse propagation in glaciers. The main features of this new formulation are: (1) the updated-Lagrangian approach that enables us to track the geometry changes in the domain dynamically using an explicit mesh-update procedure and the evolution of continuum damage at material points, without needing to include the damage advection; (2) the nonlocal gradient and integral implementations of damage that alleviate the mesh sensitivity issues inherent to local damage models; (3) the higher-order mixed finite element discretization of the Stokes equations that eliminate "checkerboard" instabilities in pressure and allow accurate and efficient computation of stress and damage fields; and (4) the automated damage controls and element removal scheme that allow us to represent fully damaged material without introducing rank deficiencies to the finite element stiffness matrix. The formulation was verified against manufactured Stokes solutions and compared with the experimentally validated small-deformation Maxwell viscoelastic model through benchmark studies. Numerical simulations performed on idealized rectangular domains demonstrate that the Stokes flow model is suitable for

simulating flow and fracture in ice as it is consistent with the Maxwell-type viscoelastic model over the shorter time scales of crevasse propagation (i.e., t=5–20 days) under gravity-induced flow. Over long decadal time scales, we expect that the proposed update-Lagrangian approach is superior to the small-deformation total Lagrangian approach due to its ability to account for large deformations. Other interesting findings from the simulation studies are: (1) the P2–P1 (Taylor–Hood) element is about as accurate as the P3–P1 element, and so it is preferable because it is computationally less expensive; whereas, the classical stabilized P1–P1 element is not as accurate; (2) the gradient damage approach predicts faster damage initiation times and crack growth rates and narrower damage zone widths compared to the Gaussian function based integral damage approach, but it is consistent with the Green's function based integral damage approach; (3) the element removal scheme simulating crack opening is consistent with the damage control strategy for  $D^{\max} = 0.999$  upon the introduction of the  $\psi$  function that relaxes the incompressibility constraint and voids the density in damage zones. Our future work will involve using the proposed formulation together with parallel computing to simulate large scale problems, such as crevasse propagation in land ice sheets with realistic geometries and boundary conditions and iceberg calving from Antarctic ice shelves.

## Acknowledgments

We gratefully acknowledge the funding support provided by the National Science Foundation's Office of Polar Programs via grants #PLR-1341428 and #PLR-1341568. We would like to thank Prof. Georg Stadler at New York University for the helpful discussions on nonlinear Stokes solvers and Prof. Kalyanababu Nakshathrala at University of Houston for the insightful discussions on stabilized mixed finite element formulations.

## Appendix A. Supplementary material

Supplementary material related to this article can be found online at http://dx.doi.org/10.1016/j.cma.2016.09.034.

#### References

- [1] A. Vieli, F.M. Nick, Understanding and modelling rapid dynamic changes of tidewater outlet glaciers: issues and implications, Surv. Geophys. 32 (4–5) (2011) 437–458.
- [2] E.M. Schulson, P. Duval, Creep and Fracture of Ice, Cambridge University Press, 2009.
- [3] J.W. Glen, The creep of polycrystalline ice, Proc. R. Soc. Lond. Ser. A Math. Phys. Eng. Sci. 228 (1175) (1955) 519–538.
- [4] J.F. Nye, The distribution of stress and velocity in glaciers and ice-sheets, Proc. R. Soc. London (1957) 113-133.
- [5] K. Cuffey, W. Paterson, The Physics of Glaciers, Elsevier Science, 2010.
- [6] C.J. van der Veen, Fundamentals of Glacier Dynamics, CRC Press, 2013.
- [7] W. Leng, L. Ju, M. Gunzburger, S. Price, T. Ringler, A parallel high-order accurate finite element nonlinear stokes ice sheet model and benchmark experiments, J. Geophys. Res. Earth Surface 117 (F1) (2012) http://dx.doi.org/10.1029/2011JF001962.
- [8] W. Leng, L. Ju, M. Gunzburger, S. Price, Manufactured solutions and the verification of three-dimensional Stokes ice-sheet models, Cryosphere 7 (1) (2013) 19–29. http://dx.doi.org/10.5194/tc-7-19-2013. URL http://www.the-cryosphere.net/7/19/2013/.
- [9] I.K. Tezaur, M. Perego, A.G. Salinger, R.S. Tuminaro, S.F. Price, Albany/felix: a parallel, scalable and robust, finite element, first-order Stokes approximation ice sheet solver built for advanced analysis, Geosci. Model Dev. 8 (4) (2015) 1197–1220. http://dx.doi.org/10.5194/gmd-8-1197-2015. URL http://www.geosci-model-dev.net/8/1197/2015/.
- [10] J. Worthen, G. Stadler, N. Petra, M. Gurnis, O. Ghattas, Towards adjoint-based inversion for rheological parameters in nonlinear viscous mantle flow, Phys. Earth Planet. Inter. 234 (2014) 23–34.
- [11] T. Isaac, G. Stadler, O. Ghattas, Solution of nonlinear Stokes equations discretized by high-order finite elements on nonconforming and anisotropic meshes, with application to ice sheet dynamics, SIAM J. Sci. Comput. 37 (6) (2015) B804–B833. http://dx.doi.org/10.1137/140974407.
- [12] J. Weertman, Bottom crevasses, J. Glaciol. 25 (91) (1980) 185-188.
- [13] C. Van der Veen, Fracture mechanics approach to penetration of bottom crevasses on glaciers, Cold Reg. Sci. Technol. 27 (3) (1998) 213–223.
- [14] C. Van der Veen, Fracture mechanics approach to penetration of surface crevasses on glaciers, Cold Reg. Sci. Technol. 27 (1) (1998) 31–47.
- [15] D.I. Benn, N.R. Hulton, R.H. Mottram, 'Calving laws', 'sliding laws' and the stability of tidewater glaciers, Ann. Glaciol. 46 (1) (2007)
- [16] F. Nick, C. Van der Veen, A. Vieli, D. Benn, A physically based calving model applied to marine outlet glaciers and implications for the glacier dynamics, J. Glaciol. 56 (199) (2010) 781–794.
- [17] J.N. Bassis, The statistical physics of iceberg calving and the emergence of universal calving laws, J. Glaciol. 57 (201) (2011) 3-16.
- [18] J. Bassis, C. Walker, Upper and lower limits on the stability of calving glaciers from the yield strength envelope of ice, Proc. R. Soc. Lond. Ser. A Math., Phys. Eng. Sci. 468 (2140) (2012) 913–931.
- [19] A. Pralong, M. Funk, Dynamic damage model of crevasse opening and application to glacier calving, J. Geophys. Res.: Solid Earth 110 (B1) (2005) 1–12.

- [20] R. Duddu, H. Waisman, A temperature dependent creep damage model for polycrystalline ice, Mech. Mater. 46 (2012) 23-41.
- [21] R. Duddu, H. Waisman, A nonlocal continuum damage mechanics approach to simulation of creep fracture in ice sheets, Comput. Mech. 51 (6) (2013) 961–974.
- [22] R. Duddu, J. Bassis, H. Waisman, A numerical investigation of surface crevasse propagation in glaciers using nonlocal continuum damage mechanics. Geophys. Res. Lett. 40 (12) (2013) 3064–3068.
- [23] M.E. Mobasher, R. Duddu, J.N. Bassis, H. Waisman, Modeling hydraulic fracture of glaciers using continuum damage mechanics, J. Glaciol. 62 (234) (2016) 794–804. http://dx.doi.org/10.1017/jog.2016.68.
- [24] D.P. Flanagan, T. Belytschko, A uniform strain hexahedron and quadrilateral with orthogonal hourglass control, Internat. J. Numer. Methods Engrg. 17 (5) (1981) 679–706.
- [25] T. Belytschko, J.S.-J. Ong, W.K. Liu, J.M. Kennedy, Hourglass control in linear and nonlinear problems, Comput. Methods Appl. Mech. Engrg. 43 (3) (1984) 251–276.
- [26] T. Elguedj, Y. Bazilevs, V.M. Calo, T.J.R. Hughes, B and F projection methods for nearly incompressible linear and non-linear elasticity and plasticity using higher-order NURBS elements, Comput. Methods Appl. Mech. Engrg. 197 (2008) 2732–2762.
- [27] A. Masud, T.J. Hughes, A stabilized mixed finite element method for Darcy flow, Comput. Methods Appl. Mech. Engrg. 191 (39–40) (2002) 4341–4370.
- [28] K. Nakshatrala, D. Turner, K. Hjelmstad, A. Masud, A stabilized mixed finite element method for Darcy flow based on a multiscale decomposition of the solution, Comput. Methods Appl. Mech. Engrg. 195 (33–36) (2006) 4036–4049.
- [29] D.Z. Turner, K.B. Nakshatrala, K.D. Hjelmstad, On the stability of bubble functions and a stabilized mixed finite element formulation for the Stokes problem, Internat, J. Numer. Methods Fluids 60 (12) (2009) 1291–1314.
- [30] D.Z. Turner, K.B. Nakshatrala, K.D. Hjelmstad, A variational multiscale NewtonSchur approach for the incompressible NavierStokes equations, Internat. J. Numer. Methods Fluids 62 (2) (2010) 119–137.
- [31] F. Brezzi, M. Fortin, Mixed and Hybrid Finite Element Methods, Springer, 1991.
- [32] B.A. Szabo, I. Babuška, Finite Element Analysis, John Wiley & Sons, 1991.
- [33] U. Brink, E. Stein, On some mixed finite element methods for incompressible and nearly incompressible finite elasticity, Comput. Mech. 19 (1) (1996) 105–119.
- [34] A.N. Brooks, T.J. Hughes, Streamline upwind/Petrov–Galerkin formulations for convection dominated flows with particular emphasis on the incompressible Navier–Stokes equations, Comput. Methods Appl. Mech. Engrg. 32 (1) (1982) 199–259.
- [35] T.J. Hughes, L.P. Franca, M. Balestra, A new finite element formulation for computational fluid dynamics: V. Circumventing the babuka-brezzi condition: a stable Petrov–Galerkin formulation of the stokes problem accommodating equal-order interpolations, Comput. Methods Appl. Mech. Engrg. 59 (1) (1986) 85–99.
- [36] T.J. Hughes, L.P. Franca, G.M. Hulbert, A new finite element formulation for computational fluid dynamics: VIII. The galerkin/least-squares method for advective-diffusive equations, Comput. Methods Appl. Mech. Engrg. 73 (2) (1989) 173–189.
- [37] L.P. Franca, S.L. Frey, T.J. Hughes, Stabilized finite element methods: I. Application to the advective-diffusive model, Computer Methods in Applied Mechanics and Engineering 95 (2) (1992) 253–276.
- [38] T.J. Hughes, Multiscale phenomena: Green's functions, the Dirichlet-to-Neumann formulation, subgrid scale models, bubbles and the origins of stabilized methods, Comput. Methods Appl. Mech. Engrg. 127 (14) (1995) 387–401.
- [39] T.J.R. Hughes, G. Sangalli, Variational multiscale analysis: the finescale greens function, projection, optimization, localization, and stabilized methods, SIAM J. Numer. Anal. 45 (2) (2007) 539–557.
- [40] Y. Bazilevs, Isogeometric analysis of turbulence and fluid-structure interaction (Ph.D. thesis), University of Texas at Austin, 2007.
- [41] D.N. Arnold, F. Brezzi, M. Fortin, A stable finite element for the stokes equations, CALCOLO 21 (4) (1984) 337–344.
- [42] C. Baiocchi, F. Brezzi, L.P. Franca, Virtual bubbles and Galerkin-least-squares type methods (Ga.L.S.), Comput. Methods Appl. Mech. Engrg. 105 (1) (1993) 125–141.
- [43] R. Duddu, L.L. Lavier, T.J. Hughes, V.M. Calo, A finite strain Eulerian formulation for compressible and nearly incompressible hyperelasticity using high-order B-spline finite elements, Internat. J. Numer. Methods Engrg. 89 (6) (2012) 762–785.
- [44] L. Foucard, A. Aryal, R. Duddu, F. Vernerey, A coupled Eulerian–Lagrangian extended finite element formulation for simulating large deformations in hyperelastic media with moving free boundaries, Comput. Methods Appl. Mech. Engrg. 283 (2015) 280–302.
- [45] C.P. Borstand, A. Khazendar, E. Larour, M. Morlighem, E. Rignot, M.P. Schodlok, A damage mechanics assessment of the Larsen B ice shelf prior to collapse: Toward a physically-based calving law, Geophys. Res. Lett. 39 (2012).
- [46] T. Albrecht, A. Levermann, Fracture-induced softening for large-scale ice dynamics, Cryosphere 8 (2) (2014) 587–605. http://dx.doi.org/10.5194/tc-8-587-2014.
- [47] E. Onate, J.M. Carbonell, Updated lagrangian mixed finite element formulation for quasi and fully incompressible fluids, Comput. Mech. 54 (2014) 1583–1596
- [48] K.-J. Bathe, E. Ramm, E.L. Wilson, Finite element formulations for large deformation dynamic analysis, Internat. J. Numer. Methods Engrg. 9 (1975) 353–386.
- [49] L.M. Kachanov, Time of the rupture process under creep conditions, Izvestia Akademii Nauk SSSR. Otdelenie Tekhnicheskich Nauk 8 (8) (1958) 26–31.
- [50] Y.N. Rabotnov, On the equations of state for creep, Progress in Applied Mechanics, the Prager Anniversary 8 (1963).
- [51] J. Lemaitre, Evaluation of dissipation and damage in metals, in: proceedings of the International Congress on the Mechanical Behavior of Materials (I.C.M.), Kyoto, Japan, 1, 1971.
- [52] J. Betten, S. Sklepus, A. Zolochevsky, A creep damage model for initially isotropic materials with different properties in tension and compression, Eng. Fract. Mech. 59 (5) (1998) 623–641.
- [53] J. Betten, S. Sklepus, A. Zolochevsky, A microcrack description of creep damage in crystalline solids with different behaviour in tension and compression, Int. J. Damage Mech. 8 (1999) 197232.

- [54] R. Duddu, H. Waisman, On the continuum damage mechanics approach to modeling of polar ice fracture: A reply, J. Glaciol. 59 (216) (2013) 799–801
- [55] J. Lemaitre, A Course on Damage Mechanics, Springer, 1992.
- [56] S. Murakami, M. Kawai, H. Rong, Finite element analysis of creep crack growth by a local approach, Int. J. Mech. Sci. 30 (7) (1988) 491–502.
- [57] D.R. Hayhurst, Creep-rupture under multi-axial states of stress, J. Mech. Phys. Solids 20 (6) (1972).
- [58] Z.P. Bazant, G. Pijaudier-Cabot, Nonlocal continuum damage, localization instability and convergence, J. Appl. Mech. 55 (2) (1988) 287–293.
- [59] G. Pijaudier-Cabot, Z.P. Bazant, Nonlocal damage theory, J. Eng. Mech. 113 (10) (1987) 1512–1533.
- [60] R. Peerlings, M. Geers, R. de Borst, W. Brekelmans, A critical comparison of nonlocal and gradient-enhanced softening continua, Int. J. Solids Struct. 38 (4445) (2001) 7723–7746.
- [61] C.V. Verhoosel, M.A. Scott, T.J.R. Hughes, R. de Borst, An isogeometric analysis approach to gradient damage models, Internat. J. Numer. Methods Engrg. 86 (1) (2011) 115–134.
- [62] M. Jirasek, P. Grassl, Evaluation of directional mesh bias in concrete fracture simulations using continuum damage models, Eng. Fract. Mech. 75 (8) (2008) 1921–1943.
- [63] R.H.J. Peerlings, M.G.D. Geers, R. de Borst, W. Brekelmans, A critical comparison of nonlocal and gradient-enhanced softening continua, Int. J. Solids Struct. 38 (44–45) (2001) 7723–7746.
- [64] R. de Borst, C.V. Verhoosel, Gradient damage vs phase-field approaches for fracture: Similarities and differences, Comput. Methods Appl. Mech. Engrg. (2016) http://dx.doi.org/10.1016/j.cma.2016.05.015. URL http://www.sciencedirect.com/science/article/pii/S0045782516303796.
- [65] J.F. Nye, The flow law of ice from measurements in glacier tunnels, laboratory experiments and the Jungfraufirn borehole experiment, Proc. R. Soc. Lond. Ser. A Math. Phys. Eng. Sci. 219 (1953) 477–489.
- [66] I.K. Tezaur, M. Perego, A.G. Salinger, R.S. Tuminaro, S.F. Price, Albany/FELIX: a parallel, scalable and robust, finite element, first-order Stokes approximation ice sheet solver built for advanced analysis, Geosci. Model Dev. 8 (4) (2015) 1197–1220.
- [67] J.M. Amundson, M. Fahnestock, M. Truffer, J. Brown, M.P. Luthi, R.J. Motyka, Ice lange dynamics and implications for terminus stability, Jakobshavn Isbr, Greenland, J. Geophys. Res. Earth Surf. 115 (F1) (2010) http://dx.doi.org/10.1029/2009JF001405.
- [68] P.L. Moore, Deformation of debris-ice mixtures, Rev. Geophys. 52 (3) (2014) 435–467, http://dx.doi.org/10.1002/2014RG000453.
- [69] T.J. Hughes, L.P. Franca, A new finite element formulation for computational fluid dynamics: VII. The stokes problem with various well-posed boundary conditions: Symmetric formulations that converge for all velocity/pressure spaces, Comput. Methods Appl. Mech. Engrg. 65 (1) (1987) 85–96.
- [70] L.P. Franca, R. Stenberg, Error analysis of Galerkin least squares methods for the elasticity equations, SIAM J. Numer. Anal. 28 (6) (1991) 1680–1697.
- [71] M. Gunzburger, R. Nicolaides, Incompressible Computational Fluid Dynamics, Cambridge University Press, 1993.
- [72] H. Zhang, L. Ju, M. Gunzburger, T. Ringler, S. Price, Coupled models and parallel simulations for three-dimensional full-stokes ice sheet modeling, Numer. Math. Theory Methods Appl. 4 (2011) 396–418.
- [73] C.R. Dohrmann, P.B. Bochev, A stabilized finite element method for the Stokes problem based on polynomial pressure projections, Int. J. Numer. Methods Fluids 46 (2004) 183–201. http://dx.doi.org/10.1002/fld.752.
- [74] C. Plate, R. Müller, A. Humbert, D. Gross, Evaluation of the criticality of cracks in ice shelves using finite element simulations, Cryosphere 6 (5) (2012) 973–984. http://dx.doi.org/10.5194/tc-6-973-2012. URL http://www.the-cryosphere.net/6/973/2012/.
- [75] A. Keller, K. Hutter, Conceptual thoughts on continuum damage mechanics for shallow ice shelves, J. Glaciol. 60 (222) (2014) 685–693.
- [76] W. Mitchell, Exact and numerical solutions for Stokes flow in glaciers (Ph.D. thesis), University of Alaska, Fairbanks, 2012.
- [77] J.A. Worthen, Inverse problems in mantle convection: models, algorithms, and applications (Ph.D. thesis), The University of Texas at Austin, 2012.